Dynamical obstruction in a constrained system and its realization in lattices of superconducting devices

Claudio Castelnovo,[1] Pierre Pujol,[1,2] and Claudio Chamon[1]

[1]*Physics Department, Boston University, Boston, Massachusetts 02215, USA*
[2]*Laboratoire de Physique, Groupe de Physique Théorique de l'École Normale Supérieure, Lyon, France*
(Received 13 November 2003; published 29 March 2004)

Hard constraints imposed in statistical mechanics models can lead to interesting thermodynamical behaviors, but may at the same time raise obstructions in the thoroughfare to thermal equilibration. Here we study a variant of Baxter's three-color model in which local interactions and defects are included, and discuss its connection to triangular arrays of Josephson junctions of superconductors with broken time-reversal symmetry and *kagomé* networks of superconducting wires. The model is equivalent to an Ising model in a hexagonal lattice with the additional constraint that the magnetization of each hexagon is ± 6 or 0. Defects in the superconducting models correspond to violations of this constraint, and include fractional and integer vortices, as well as open strings within two-color loops. In the absence of defects, and for ferromagnetic interactions, we find that the system is critical for a range of temperatures (critical line) that terminates when it undergoes an exotic first-order phase transition with a jump from a zero magnetization state into the fully magnetized state at finite temperature. Dynamically, however, we find that the system becomes frozen into domains. The domain walls are made of perfectly straight segments, and domain growth appears frozen within the time scales studied with Monte Carlo simulations, with the system trapped into a "polycrystalline" phase. This dynamical obstruction has its origin in the topology of the allowed reconfigurations in phase space, which consist of updates of closed loops of spins. Only an extreme rare-event dominated proliferation of confined defects may overcome this obstruction, at much longer time scales. Also as a consequence of the dynamical obstruction, there exists a dynamical temperature, lower than the (avoided) static critical temperature, at which the system is seen to jump from a "supercooled liquid" to the polycrystalline phase within our Monte Carlo time scale. In contrast, for antiferromagnetic interactions, we argue that the system orders for infinitesimal coupling because of the constraint, and we observe no interesting dynamical effects.

I. INTRODUCTION

Systems with hard constraints often display interesting thermodynamic properties such as infinite-order phase transitions or, on the contrary, very sharp first-order phase transitions. Many of these models can be described in terms of vertex models and some of them are exactly solvable. Examples of such systems are given by dimer models,[1] the planar ice model,[2] or the three-coloring model of the hexagonal lattice.[3]

It is very natural to ask whether the hard constraint, which leads to the interesting thermodynamics, may at the same time pose obstructions in the (possible) path to thermal equilibration. In essence, equilibrium properties require averages over all the configurations allowed by the constraint, weighted in accordance with the appropriate Boltzmann-Gibbs distribution. Dynamically, the system must sample the different allowed states in a manner that satisfies detailed balance. However, leaping from an allowed configuration to another might require large rearrangements, and physically one must investigate which mechanisms could possibly lead to these moves in phase space and what are the corresponding time scales. Sometimes the constraint forbids any local rearrangement of the system (as in the present case), and it ought to be softened in order to allow for a local dynamics. The system then evolves by formation of constraint-violating defects that propagate and recombine.

Plenty of issues arise regarding the dynamical generation and recombination of defects, which depend on the microscopic details of the physical system, and the energetics of the states outside the manifold of constraint-satisfying states. For example, paying the energy cost to create a defect already slows down the dynamics; however, this waiting for the defect generation simply rescales the time scales for dynamical evolution in a trivial way. More interesting are those issues related to the possible energy costs for moving defects around. In particular, if the microscopics are such that the defects (when created in pairs) are confined, one would expect further and nontrivial slowing down of the dynamics.

Glassy behavior in constrained three-color models with infinite range interactions has indeed been recently found by Chakraborty, Das, and Kondev.[4] This is an interesting example of glassy behavior in a Hamiltonian model without quenched disorder, where it was found that the characteristic time scales obeyed a Vogel-Fulcher law as the temperature approached a dynamical transition temperature, mimicking fragile structural glasses. In order to maneuver within the phase space of allowed states, nonlocal loop dynamics was implemented.

In this paper, we study variations of the Baxter three-color model with short-range interactions and discuss the possible mechanism for defect motion. In particular, we argue that the loop updates used by Chakraborty *et al.*[4] correspond to the unbinding of certain defect pairs that are deconfined, and thus they are the least costly mechanism for dynamical evo-

lution. We find that finite range ferromagnetic interactions lead to a frozen "polycrystal," as opposed to a fragile glass as in the case of infinite range interactions. We present two possible experimental realizations using lattice arrays of superconducting devices that could in principle be experimental settings for studying sluggish relaxation or nonequilibrium effects in Hamiltonian systems without quenched disorder.

In Sec. II we present in detail the three-color model, and show that it is equivalent to an Ising model on a hexagonal lattice, with the constraint that the magnetization of each hexagon must be ± 6 or 0. In the Ising language the extra interaction that we add to the three-color model has a simple form: it is a nearest-neighbor spin-spin interaction. Such interaction is present in the possible experimental realizations of the model in two different two-dimensional (2D) superconducting geometries. Because of the constraint imposed on the plaquettes, the system is critical in the absence of two-spin interactions ($J=0$) and is described by a $c=2$ conformal field theory (CFT).[5] In Sec. III, we use this description to argue about the behavior of the model in the presence of nonzero two-spin interactions. While for arbitrarily small antiferromagnetic coupling ($J<0$) the system orders, it remains critical for small ferromagnetic coupling ($J>0$). The CFT description near the $J=0$ point is ill suited for strong couplings. In this regime we use instead a cluster mean-field method (CMFM) which has proven to be very accurate in describing constrained system such as the ice model.[6] We find a strong first-order phase transition where the system jumps from the disordered configuration to the fully magnetized ferromagnetic state (FMFS).

When the hard constraint is softened, defects are allowed in the system at a high-energy scale U, which enters in the defect formation energy and in the defect pair interactions. In Sec. IV, we discuss the role of these defects and their implications in the dynamics of the system. In the superconducting realizations there are a number of different defects: fractional vortices, integer vortices, and open segments of closed two-color loops. Integer and fractional vortices can be shown to be confined below a Kosterlitz-Thouless transition temperature that can be rather high depending on the energy scale U. Thus, these defects are rather ineffective as a mechanism to move from one allowed state to another. We show, on the other hand, that the end points of open segments of closed loops made of two alternating colors are deconfined, they can move around and travel a whole closed loop, and therefore they are the main actors for the evolution of the system. For defect formation rates much smaller than the defect recombination rates, this evolution corresponds essentially to the loop dynamics that we use in the present paper.

In Sec. V we study the dynamics of the constrained system. By fitting the value of the free energy for the disordered state as a function of temperature and comparing it to the one of the ordered state we first obtain an accurate estimate for the transition temperature, which is in good agreement with the result from the CMFM. We then show that there is no sign of the above-mentioned thermodynamic transition to the FMFS. The system instead becomes supercooled and undergoes a lower-temperature nonequilibrium transition from the supercooled liquid phase to a frozen "polycrystalline" phase. The transition shows features that are characteristic of first-order phase transitions, such as a hysteretic behavior as a function of temperature. The underlying physics behind this phenomenon is understood by studying the spin-spin autocorrelation function as well as the evolution of the internal energy and other physical quantities when we cool the system at different cooling rates or after a quench from infinite temperature.

II. THE MODEL AND ITS POSSIBLE EXPERIMENTAL REALIZATIONS

In this section we review Baxter's three-color model, and present two of its possible experimental realizations in lattices of superconducting devices in some detail. We show that the three-color model and these two realizations can be described as an Ising model on a hexagonal lattice, with a plaquette constraint of $\pm 6,0$ for the sum of the spins around each hexagon. It is important to notice that while the three-color model is only $\mathbb{Z}_2$ symmetric in the Ising spin representation, the superconducting realizations have a larger $\mathbb{Z}_2 \times U(1)$ symmetry due to the superconducting phase. This difference is particularly relevant for the possible defects that can originate in an allowed configuration and for their dynamic behavior.

The one extra ingredient that we add to Baxter's three-color model is a local interaction. In the Ising spin representation, this interaction takes the form of a nearest-neighbor spin-spin interaction. It has the effect, in the three-color model, of favoring or opposing to the alignment of bonds of the same color on neighboring sites. The extra interaction is responsible for all the interesting thermodynamical and dynamical effects that are studied in this paper. Moreover, in the lattices of superconducting devices these interactions are always present.

A. The three-color model

The three-color model consists of vertices having three bonds of different colors: A, B and C. These different colors can be thought of as three different phases differing pairwise by $\pm 2\pi/3$, which is how we will later connect the model to arrays of superconducting devices. One can naturally associate to each vertex a chirality spin ± 1 depending on the counterclockwise or clockwise ordering of the phases, as shown in Fig. 1. A hexagonal lattice is constructed with these vertices by connecting the bonds, where the connected bonds must share the same color. As we show below, the chirality spins cannot adopt an arbitrary configuration. Indeed, the spins must satisfy the constraint that their sum around any hexagon of the lattice is $\pm 6,0$. On the other hand, given an allowed configuration of the spins, there are clearly three different corresponding color configurations, since any global even permutation of the colors in the lattice gives rise to the same spin configuration. In the absence of any kind of interaction this model corresponds to the Baxter's three-coloring model on the hexagonal lattice. The partition function Z has a purely entropic origin and its value is given by
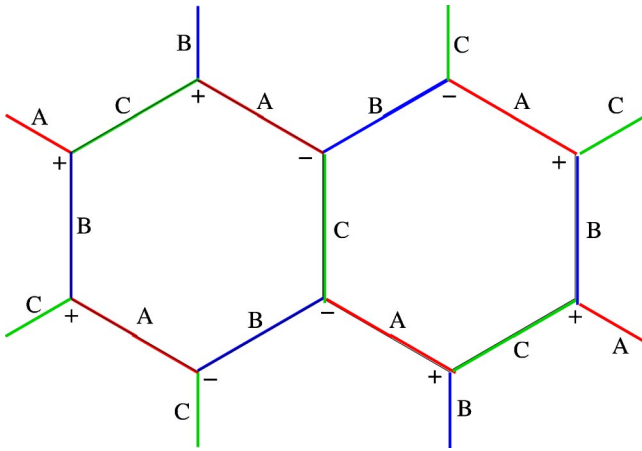
FIG. 1. (Color online) The gluing of the ABC vertices gives Baxter's three-coloring model on the hexagonal lattice. To every vertex we can associate a chirality spin depending on the order in which the three colors appear counterclockwise around the vertex: $+/-$ for even/odd permutations of the sequence ABC.
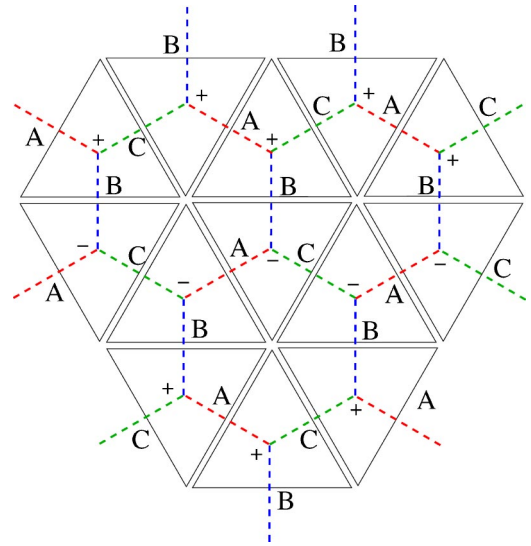

FIG. 2. (Color online) An example of the correspondence between the Josephson-junction array and the three-color model, provided we identify the three colors with the values of the phases of the order parameter in the middle of each triangle edge. Notice that ferromagnetic order among nearest-neighboring spins corresponds to aligning the bonds with the same color along the same direction.

the number of ways of coloring the bonds of the hexagonal lattice. This number is known to grow exponentially with the system size. Indeed, Baxter solved exactly this model and showed that $Z = W^N$ for large values of the number of sites N, where $W = 1.2087 \ldots$ is the entropy per site.[3]

It is worth discussing in detail how the system can rearrange from one allowed configuration to another. No single-bond flip or double-bond exchange is allowed without violating the constraint in the neighboring vertices. However, we can notice that by choosing one vertex and two colors, say A and B, we can uniquely define a loop by taking the sequence of ABAB . . . bonds starting from the chosen vertex. The loop must be non-self-intersecting and closed, the last property holding only if the system has periodic boundary conditions. Clearly, if we pick one such loop and we flip the color sequence, say ABAB . . . to BABA . . . , the color constraint is preserved. These loop flips (or updates) provide a mechanism for the system to move around the phase space of allowed configurations. In Sec. IV we will show how the loop updates originate from local constraint-violating defects.

Notice that, given any allowed configuration, every vertex belongs to one and only one of such loops. Thus, by simply removing all the bonds of one of the three colors (say C), we realize one of the three possible simultaneous mappings of the system to a fully packed loop configuration on the hexagonal lattice which, at large scales, can be described by an SU(3) level 1 Wess-Zumino-Novikov-Witten (WZNW) model.[5]

The three-color model becomes even richer when we introduce a nearest-neighbor spin-spin interaction in the Ising representation, which we do in Sec. II E, after we discuss the experimental realizations right below.

B. The Josephson-junction array of superconductors

A possible experimental realization of the model is given by a Josephson-junction array of triangles of a supercon-

ductor with broken time-reversal symmetry. For example, there is experimental evidence of a $p_x \pm i p_y$ order parameter in the compound Sr_2RuO_4;[7,8] here the two possible states $p_x \pm i p_y$ correspond to the chirality spin ± 1 defined above. The same geometry we propose here with $p \pm i p$ states has also been studied by Moore and Lee, who in addition to the p-wave states have also looked at $d \pm i d$ superconductors,[9] believed to be realized by the recently discovered hydrated cobalt oxide compounds. In their work, they have also discussed other type of arrays in triangular and square lattices.

In the $p_x \pm i p_y$ Josephson-junction arrays, the three colors correspond to the three relative phases of the order parameter in the middle of each of the edges of the triangles, which differ by $\pm 2\pi/3$ (see Fig. 2). (To be precise, the phase of the order parameters is defined in momentum space; but, as it can be deduced from the analysis carried out in the Appendix, one can think in real space by considering the phases for the momenta that point along the directions perpendicular to the three faces of each triangle.) The superconducting order parameter of each triangle has also an overall U(1) degree of freedom. Therefore, at the center of each of its three edges, one can define a phase $\theta_{i,a} = \theta_i \pm (2\pi/3)a$ for the triangle at site i, along its ath edge ($a = 0, 1, 2$), where the edges are labeled counterclockwise starting from the horizontal one (see Fig. 3). The $\pm$ sign corresponds to the chirality $\sigma_i = \pm 1$ of the $p_x \pm i p_y$ state at site i. The Josephson coupling $-U \cos(\theta_{i,a} - \theta_{j,a})$ along an edge shared by two neighboring triangles tends to align the phases $\theta_{i,a}$ and $\theta_{j,a}$. In the $U \rightarrow \infty$ limit one recovers Baxter's three-coloring model, modulo a global U(1) phase. Notice that, in this infinite U coupling limit, the only difference between this system and the three-color model (in the spin representation) described in the preceding section is a $\mathbb{Z}_2 \times U(1)$ symmetry instead of a simple $\mathbb{Z}_2$ symmetry. We will show in Sec. IV how this dif-
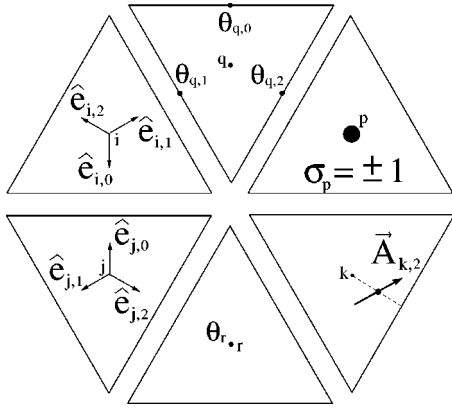
FIG. 3. Labeling of the edges of the up and down triangles, with the relative unit vectors $\hat{e}_{i,a}$. While the chirality spins σ_p sit at the centers of the triangles, the "gauge" fields (an example of which is shown in one of the triangles) sit at the midpoints of the segments joining the centers of the triangles to the corresponding edges. Examples of the U(1) phase θ_r and of the edge phases $\theta_{q,a}$, $a = 0,1,2$ are also shown.

ference allows for a wider variety of defects in the Josephson-junction array rather than in the three-coloring model.

C. The kagomé network of superconducting wires

Another (related) realization of the three-color model is given by a superconducting *kagomé* wire network in the presence of a magnetic field[10–12] such that the magnetic flux per triangular plaquette is one-half of a flux quantum ($f = 1/2$). Using a Ginzburg-Landau analysis, Park and Huse[12] showed that the possible superconducting phases must have a gauge-invariant phase change around each elementary triangle equal to $\pm\pi$ and a gauge-invariant phase change along each wire segment equal to $\pm\pi/3$. They also show that the allowed minimum free-energy states of this model are equivalent to ground states of the *XY* kagomé antiferromagnet, which are in one-to-one correspondence to the three-color model configurations, modulo a U(1) phase analogous to the one in the Josephson-junction array. The ± 1 chirality spin can be immediately read from the value of the (counterclockwise) phase change around each triangle $\pm\pi$, i.e., from the value of the induced flux through each triangle: 0 or 1 flux quantum. Even though this realization seems quite similar to the previous one, there are differences that arise mainly from the fact that time reversal is explicitly broken by the external field in the wire networks. For example, the $\pm\pi$ chiralities do not have the same energy in the case of wires of finite width. We refer the reader to the thorough discussion of the energetics by Park and Huse.[12]

D. Mapping to a constrained Ising model

The hard constraint of the three-color model imposes a hard constraint in the allowed configurations of the chirality ± 1 Ising spins. Here we show that in the spin representation the hard constraint requires that any elementary hexagonal plaquette P must have total magnetization:

$$\sigma_P^\bigcirc = \sum_{i \in P} \sigma_i = \pm 6,0. \tag{1}$$

A similar result was obtained by Di Francesco and Guitter when connecting the folding problem in the triangular lattice to the three-coloring model.[13] In our proof, we make use of phases accumulated along paths on the hexagonal lattice, requiring that these phases are single valued. This approach is more appropriate to the discussion of superconducting systems and their defects (integer and fractional vortices) that we present in this paper.

Indeed, as we show, one can obtain a simple interpretation of the hard constraint by identifying the accumulated phase around any loop lying on links of the hexagonal lattice with the circulation of a vector potential. For concreteness, we will use the example of the Josephson-junction array in the discussion, but the argument is general.

The phase $\theta_{i,a}$ on the edge a of the superconducting triangle i can be written as

$$\theta_{i,a} = \theta_i + \hat{e}_{i,a} \cdot \vec{A}_{i,a}, \tag{2}$$

where $\hat{e}_{i,a}$ is the unit vector that points from the center of triangle i to its ath edge, and the "gauge" potential $\vec{A}_{i,a}$ is defined at the center of such segment (see Fig. 3).

The phase difference across a face a between triangles i and j is

$$\theta_{i,a} - \theta_{j,a} = \theta_i - \theta_j + [\hat{e}_{i,a} \cdot \vec{A}_{i,a} - \hat{e}_{j,a} \cdot \vec{A}_{j,a}]. \tag{3}$$

The last term is simply the discrete sum equivalent of $\int d\vec{\ell} \cdot \vec{A}$ (notice that for neighboring sites i,j the unit vectors are opposed, $\hat{e}_{i,a} = -\hat{e}_{j,a}$).

Now recall that one can write $\theta_{i,a} = \theta_i + (2\pi/3)a\,\sigma_i$ and hence the vector potential is such that

$$\hat{e}_{i,a} \cdot \vec{A}_{i,a} = \frac{2\pi}{3}a\sigma_i. \tag{4}$$

What is the corresponding magnetic field? This is simple to answer, by looking at the accumulated phase around a loop. Consider an elementary counterclockwise hexagonal loop. The loop visits six triangles, and the portion of the loop within each triangle enters through face a and exits through face $a-1$ (mod3), so that the accumulation of the vector potential along that portion of the loop is

$$\hat{e}_{i,a-1} \cdot \vec{A}_{i,a-1} - \hat{e}_{i,a} \cdot \vec{A}_{i,a} = \frac{2\pi}{3}(a-1)\sigma_i - \frac{2\pi}{3}a\sigma_i$$

$$= -\frac{2\pi}{3}\sigma_i. \tag{5}$$

The above result, that each of the six sites visited by an elementary hexagon loop contributes $-(2\pi/3)\sigma_i$ to a counterclockwise accumulation of phase around the loop, has a very simple interpretation. Each Ising spin $\sigma_i = \pm 1$ corresponds to a $\mp 2\pi$ vortex sitting at a vertex of the hexagonal lattice. Each vertex is shared by three hexagons; hence each hexagon can be thought to contain 1/3 of that vortex, as
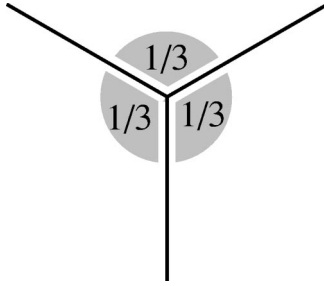
FIG. 4. A vortex sitting at each vertex in the hexagonal lattice is shared by three hexagons. Hence, the contribution to a counter-clockwise accumulation of phase around a hexagon encloses one-third of each of the six vortices sitting at the six vertices in the loop.

depicted in Fig. 4. This is why the contribution from the hexagonal path going through vertex i picks up the phase $-(2\pi/3)\sigma_i$ as shown above. Basically, the vortex is divided equally among the three neighboring hexagons sharing the common vertex.

Using Eq. (5) we can now compute the flux encircled by an elementary hexagon on plaquette P; it is given by

$$\Phi_P^\circ = -2\pi/3 \sum_{i \in P} \sigma_i = -2\pi/3\sigma_P^\circ. \tag{6}$$

Therefore the flux enclosed by an elementary hexagonal loop is just 1/3 of the sum of the vorticities in the six sites. Now, matching the color scheme after going around any closed loop requires the phase around any hexagon to be uniquely defined (mod2π), which in turn requires the flux to be a multiple of 2π: $2\pi/3\ \sigma_P^\circ = 0$ (mod2π), that is, $\sigma_P^\circ = \pm 6, 0$ (notice that σ_P° is even). Since the total flux inside any loop is given by the sum of the fluxes through each elementary hexagon, then the condition $\sigma_P^\circ = \pm 6, 0$ grants the phase to be uniquely defined (mod2π) around any loop.

Once the $\sigma_P^\circ = \pm 6, 0$ constraint is satisfied, there is a one-to-three mapping of any spin configuration to a configuration of the color model, since there are three even permutations of the colors that produce the same chirality spin configuration.

In the case of the kagomé wire networks at half-flux *per* triangle (or vertex of the hexagonal lattice), each triangle will accommodate either 0 or 1 vortex. So instead of $\sigma_i = \pm 1$ one has a variable $n_i = 0, 1$. Still, the vortices are split equally into three pieces, and the circulation around a hexagonal plaquette P going through the centers of the kagomé triangles is $(2\pi/3)N_P^\circ = (2\pi/3)\Sigma_{i \in P} n_i$. The circulation is a multiple of 2π if $N_P^\circ = 6, 3, 0$. Indeed, the fact that the vortices in the elementary triangles are shared by three sites was used by Park and Huse[12] in their argument for fractionalized vortices in the kagomé superconducting wire networks.

For finite U, there are defects that violate the $\sigma_P^\circ = \pm 6, 0$ constraint; we shall discuss these defects in detail in Sec. IV, where we study integer and fractional vortices, as well as open segments of closed two-color loops. We analyze whether these different defects are confined or deconfined, and their importance in determining the ilk of the processes responsible for the dynamics.

E. Interactions

Each experimental realization of our model contains sub-dominant effects that may lead to a degeneracy lifting of the ground state. In this paper we concentrate on the effect produced by nearest-neighbor interactions between the chirality spins:

$$H = -\sum_{\langle i,j \rangle} J\sigma_i \sigma_j, \tag{7}$$

where the coupling J depends on the microscopic details of the problem. Such a coupling can arise, for example, if one considers the higher-order effects of having an extended Josephson-junction barrier between two neighboring triangles in the array geometry. In the Appendix we show how to derive the constants U and J from a microscopic Hamiltonian for the array of Josephson couplings and we discuss the conditions for having $U \gg J$. The sign of the J coupling is positive in this case.

This nearest-neighbor interaction leads, in the color language, to an aligning or antialigning interaction between the bonds, depending on the sign of the coupling constant J as it can be easily seen with the help of Fig. 2. For J positive, the spin interaction is ferromagnetic and the zero-temperature ground state (g.s.) of the system has all the bonds with the same color aligned in the same direction. We will refer to this translation invariant state as the FMFS state or single crystal state. For J negative, the spin interaction is antiferromagnetic and the zero-temperature g.s. of the system is a configuration where the six bonds in every hexagon form a sequence of only two alternating colors, which is simply the Néel order in the hexagonal lattice.

In the following section, we discuss the thermodynamics of this system considering only the phase space of the configurations allowed by the ABC coloring constraint or, equivalently, by the $\sigma_P^\circ = \pm 6, 0$ constraint.

III. THERMODYNAMICS OF THE DEFECT-FREE MODEL

A. Small J and the CFT description

Since the model without interactions can be described by a WZNW CFT, it is tempting to use this technique to analyze its behavior for small values of the spin-spin interaction.

The first step is to represent the system by a height model (see Kondev *et al.* for details[5]). Flat configurations of this height model correspond to the different Néel states of the system. In terms of the colors there is a total of six of those configurations which are arranged to form an hexagonal lattice. The coarse-grained version is described by two fields $\vec{h} = (h_1, h_2)$ and a locking potential $V(\vec{h})$ that favors the fields to lie in one of the flat configurations; this potential has then the periodicity of the hexagonal lattice. The action reads

$$S = \int d^2 x \left(\frac{\pi}{2} \left| \boldsymbol{\nabla} \vec{h} \right|^2 + V(\vec{h}) \right). \tag{8}$$

In this language, the spin-spin interaction introduces a perturbation which is proportional to the "locking potential" since, depending on the sign of J, it favors or opposes the

locking in one of the flat configurations. In the WZNW language, the locking potential can be written as a current-current perturbation of the underlying WZNW model.[5]

When the spin-spin interaction is turned on, we can use this description to propose an action for the perturbed CFT. Since the A,B,C permutation symmetry is preserved, we can argue that the perturbing term to the pure CFT action should read

$$\int d^2x \left[\lambda_H \left(\sum_{i=1}^{2} J_R^{H_i} J_L^{H_i} \right) + \lambda_E \left(\sum_{j=1}^{3} J_R^{\alpha_j} J_L^{-\alpha_j} + J_R^{-\alpha_j} J_L^{\alpha_j} \right) \right],$$
(9)

where α_j's are the generators of the root lattice of su(3), and the Cartan generators J^{H_i} are simply given by the derivatives of the height fields ∂h_i. The case $\lambda_E = \lambda_H$ corresponds to the SU(3) symmetric case. The one-loop renormalization-group (RG) equation in this case reads

$$\dot{\lambda} = -\frac{3}{2\pi} \lambda^2,$$
(10)

and for $\lambda > 0$ the flow is toward the unperturbed level 1 SU(3) WZNW model, which can be identified with the $J = 0$ case. In general, however, we just have the A,B,C permutation symmetry, and we cannot exclude the possibility of $\lambda_H \neq \lambda_E$. Defining $\delta\lambda = \lambda_H - \lambda_E$, the RG is now

$$\dot{\delta\lambda} = \frac{1}{\pi} \, \delta\lambda \, \lambda_E,$$

$$\dot{\lambda}_E = -\frac{3}{2\pi} \lambda_E^2 - \frac{1}{\pi} \, \delta\lambda \, \lambda_E,$$
(11)

where, at least for a small spin-spin interaction, we assume $|\delta\lambda| \ll \lambda_E$. The RG flow is as follows (see Fig. 5). For $\delta\lambda > 0$, the system flows to the line of fixed points $\lambda_E = 0$. While the SU(3) symmetry is broken, the system remains critical. We propose that this case corresponds to a ferromagnetic interaction, since it is equivalent to a decrease of the locking potential. This result is valid for small interspin couplings. As we show below, for large enough couplings a first-order phase transition takes place. Since this is highly nonperturbative in the CFT language, this scenario is much better described by the cluster mean-field method that we explain below. For an antiferromagnetic coupling, $\delta\lambda < 0$ and the flow goes toward strong coupling, bringing the system off criticality and forcing the system into antiferromagnetic ordering, as was argued by Huse and Rutenberg[14] in their studies of the related classical kagomé *XY* model.

B. The cluster mean field method: General approach

The CMFM is a technique that has proven to be very powerful in studying structural phase transitions in crystals and the thermodynamics of vertex models.[6] When a system is constrained, fluctuations are considerably reduced and an appropriate mean-field treatment can give very good results if the constraint is taken into account. The idea is to consider as the fundamental entity coupled to a ''molecular'' field,
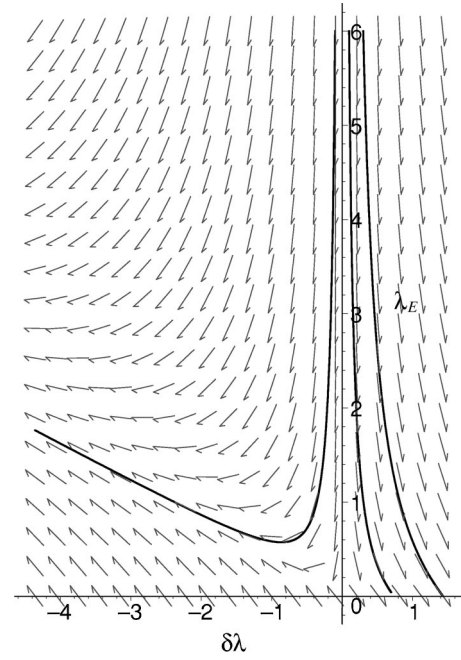

FIG. 5. Diagram of the RG flow for our model, where the horizontal axis corresponds to $\delta\lambda$ and the vertical to λ_E. The solid lines are numerical solutions of the system of equations (11) for three different initial conditions, and are drawn for visualization purposes only.

instead of a single spin, a cluster in which the allowed spin configurations are restricted by the constraint. The bigger the cluster, the more accurately fluctuations and constraints are taken into account. This method has given very precise results for the ice model[6] and is a good candidate for giving an accurate picture of our constrained spin model in the hexagonal lattice.

It is particularly simple to introduce the CMFM in the case of a corner sharing plaquette[15] lattice with Hamiltonian

$$H = \sum_{i,j} J_{i,j} \sigma_i \sigma_j + h \sum_i \sigma_i,$$
(12)

where the range of the $J_{i,j}$ interaction is shorter than the distance between the two farthest spins in a plaquette. This is the case for the present system. Let us assume that the lattice has N spins and $2N/S$ plaquettes, where each plaquette has S sites. The sums in the Hamiltonian can be rearranged as

$$H = \sum_P \left[\sum_{i,j \in P} J_{i,j} \sigma_i \sigma_j + h \sum_{i \in P} \sigma_i \right] - h \sum_i \sigma_i,$$
(13)

where the first sum is over all plaquettes P and the last term compensates for the double counting of the site energy term. The mean-field approximation is obtained by considering each term as the sum over an elementary cluster (of S and 1 spins, respectively) coupled to an effective field representing the interaction with the rest of the lattice:

$$H \simeq \frac{2N}{S}\left[\sum_{i,j\in P} J_{i,j}\sigma_i\sigma_j + (h+\phi_{ext})\sum_{i\in P}\sigma_i\right] - N[(h+\phi)\sigma_i]$$

$$= \frac{2N}{S}H_S - NH_1, \tag{14}$$

where H_S and H_1 are the S- and 1-spin cluster Hamiltonian, respectively. Here, ϕ and ϕ_{ext} are proportional to the number of spins that are external to the cluster but connected to the internal spins. Since for the 1-spin clusters such number of external spins is twice the number for the S-spin clusters, we have $\phi = 2\phi_{ext}$. Let us now define the effective internal energy per spin

$$\varepsilon = \frac{2}{S}\langle H_S\rangle_S - \langle H_1\rangle_1, \tag{15}$$

where $\langle\cdots\rangle_S$ and $\langle\cdots\rangle_1$ are the thermal averages computed with H_S and H_1, respectively. Integrating then over the inverse temperature β we get an effective free energy:

$$\beta F = -\frac{2}{S}\ln Z_S + \ln Z_1, \tag{16}$$

where $Z_i = \mathrm{Tr}\{\exp(-\beta H_i)\}$, $i = S, 1$, and the integration constant has been chosen such that in the case of unconstrained spins we get the trivial entropy $\ln(2)$ at infinite temperature. Minimizing the effective free energy with respect to ϕ:

$$\frac{\partial F}{\partial \phi} = 0 \tag{17}$$

is equivalent to imposing the self-consistency equation for the magnetization:

$$\langle\sigma\rangle_S = \langle\sigma\rangle_1 \tag{18}$$

and it gives us the optimal value for the field ϕ, which determines the behavior of the system at a given temperature. An important benefit of this method is the fact that it can be extended to larger and larger clusters. This allows us to improve systematically the accuracy of the results.

C. Application of the CMFM to the defect-free model

In order to be able to apply the CMFM to our problem in a straightforward way, it is convenient to switch to a bidual representation and describe our system in terms of spins $S_{ij} = \pm 1$ sitting on the links of the hexagonal lattice (see Fig. 7). These spins are given by the product of the original chirality spins σ_i at the two vertices of each link: $S_{ij} = \sigma_i\sigma_j$. Obviously, the number of configurations of the S spins is half the number of original σ spin configurations, due to the $\mathbb{Z}_2$ invariance of the product $\sigma_i\sigma_j$. The advantage of this mapping is that our lattice becomes now the (corner sharing hexagons) kagomé net in which each spin S_i is shared by two elementary plaquettes. In this description, the Hamiltonian (7) restricted to the nearest-neighbor interaction reads simply
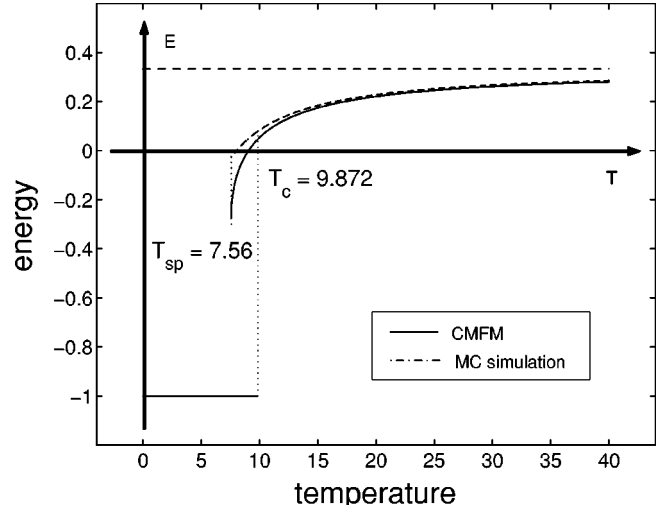

FIG. 6. Plot of the internal energy per link as a function of the temperature (in units of the coupling constant J). The solid line is the prediction from the CMFM and the doted-dashed line is the result from the numerical simulation.

$$H = -J\sum_\alpha S_\alpha, \tag{19}$$

where the index α refers to a link of the hexagonal lattice or a site of the bidual kagomé lattice. The CMFM implementation is particularly easy since in this picture we just have an effective magnetic field J in Eq. (12). The clusters that we use are the single-spin cluster and the elementary hexagon cluster (with 11 different configurations for the S spins), and the corresponding partition functions are given by

$$Z_1 = ax^2 + 1/(ax^2),$$

$$Z_6 = a^6x^6 + a^{-6}x^{-6} + 3(ax)^2 + 6/(ax)^2, \tag{20}$$

where $a = e^{\beta J}$ and $x = e^{\beta\phi/2}$. We can now obtain the values ϕ_{opt} corresponding to the minima of the effective free energy. Notice that ϕ_{opt} determines the equilibrium value of $\langle S\rangle$, i.e., of the internal energy per link of the original system. This method predicts the following scenario: for $T \to \infty$ we have $\langle S\rangle = 1/3$, which corresponds to an antiferromagnetic coupling in the system solely due to the constraint. This nontrivial value of the energy density is very close to the result obtained with the numerical method (see Sec. V). The cluster mean-field method also gives a reasonable estimate for Baxter's entropy in the limit $T \to \infty$. Substituting Eq. (20) into Eq. (16) and taking the limit $T \to \infty$ we obtain the entropy per site $S = \ln(11/8)/2 \simeq 1.1726$, while the exact value is $1.2087 \dots$. Since the analytical expressions for the forthcoming quantities are too cumbersome, we just mention here their numerical values. At $T \simeq 9.872J$ the system undergoes a first-order phase transition in which the energy density jumps from $\langle S\rangle \sim 0.05$ to a fully polarized state in which $\langle S\rangle$ is exactly -1 (see Fig. 6). This transition has been first noticed via transfer matrix analysis by Di Francesco and Guitter[16] in the context of a folding transition. Our CMFM result is very close to their estimated critical temperature

(9.1J) and even closer to our Monte Carlo estimate 9.6J (see Sec. V A 1). In terms of the original spins, this behavior corresponds to the exotic scenario in which the magnetization jumps from 0 to the fully saturated value 1 at the critical point, as was argued by Di Francesco and Guitter.[16] A similar kind of transition is also found in a frustrated spin model on the triangular lattice,[17] which turns out to be equivalent to a dimer model on the hexagonal lattice. Such kind of transition is accompanied by slow dynamics and aging. As we will see below, slow dynamics is also a central issue in our case.

Another temperature that we can compute via the CMFM is the spinodal temperature of the system. This is typical of first-order phase transitions, where an appropriate fast cooling process can avoid crystallization and bring the system into a supercooled liquid phase. The spinodal temperature T_{sp} is the temperature at which the supercooled liquid becomes unstable due to the crystal nucleation process. In this case, we can study the shape of the CMFM effective free energy as a function of ϕ for different temperatures. Starting from $T \sim \infty$ and lowering the temperature, the minimum corresponding to the liquid phase first becomes a local minimum (metastability) and eventually disappears. This metastability limit corresponds to the spinodal temperature $T_{sp} \simeq 7.56$ of the present model.

The choice of the bidual spin representation to implement the CMFM is due to the fact that the system becomes a model for which the CMFM is particularly suitable. Indeed, in terms of the bidual spins, the system becomes a kagomé lattice seen as an array of corner sharing hexagons, in which now the new spins are sitting at the vertices. By associating to each of the 11 configurations for each hexagon its corresponding energy, the model can also be described as an 11 vertex model on the triangular lattice dual to the hexagonal. This choice of variable usually limits the analysis since it does not allow us to measure the magnetization of the system, which is the typical order parameter used to study phase transitions. In the present case however the energy density variable gives very good results in the characterization of the system since the transition is first order. For continuous phase transitions the situation is different. Even though the CMFM still gives a quite accurate result for the numerical value of the energy density (in contrast to the normal mean-field method), it may fail in reproducing a subtle behavior such as an infinite slope point at T_c in the energy vs temperature curve. In this case, measuring the magnetization of the system is a much more powerful tool to detect and study the second-order phase transition. Thus, one needs to get back to the original spins instead of the bidual ones. Implementing the CMFM technique within the context of the real spins has two main disadvantages in our case. On one hand, the spins do not form corner sharing plaquettes, and relating the mean fields acting on the one-spin cluster and on the six-spin cluster becomes more difficult. On the other hand, since the coupling J is a two-spin nearest-neighbor interaction, a single variational mean field cannot take simultaneously into account both the J interaction (for which each spin interacts with its three neighbors) and the effective interaction due to the constraint (for which each spin interacts with all the 12 spins belonging to the three adjacent hexagons).

D. Free-energy argument for a first-order phase transition

The key point for understanding this particular phase transition is to understand the very peculiar nature of its FMFS ground state. As we already discussed before, in the FMFS state all the bonds of the same color are aligned in the same direction. As a result, any two-color loop is maximally straight and winds around the whole system. Thus, the smallest possible rearrangement of the FMFS configuration that produces another allowed configuration is the update of one of such loops. This is a striking feature of the ferromagnetic three-coloring model: the g.s. is separated from the first (1-loop) "excited" state by a system-spanning update which costs an energy: $E_{\text{1-loop}} - E_{\text{FMFS}} = 2JL$, where $E_{\text{FMFS}} = -3JL^2$ and L is the system size ($2L^2$ sites, $3L^2$ bonds). Notice that if one prepares the system in the $T=0$ FMFS and starts to heat, the system is likely to remain in that state even for $T \rightarrow \infty$ for fast enough heating rates. Indeed, such an energy separation is likely to make the FMFS state metastable even for $T \rightarrow \infty$, in the thermodynamic limit. Since the FMFS state has zero entropy and the entropy of a straight winding loop is $\ln(3L)$, we can write the free energies of the two states

$$F_{\text{FMFS}} = -3JL^2,$$

$$F_{\text{1-loop}} = -3JL^2 + 2JL - T\ln(3L). \qquad (21)$$

Clearly in the thermodynamic limit the energy cost $\Delta E \sim L$ overwhelms the entropic gain $\Delta S \sim \ln L$ and the excited state will never be favored over the FMFS state at any temperature. A similar argument applies to higher excited states, as long as their entropy is not exponential in the system size. The system is incapable (at equilibrium) to move out of its ground state in a "smooth way." In terms of configurations, it has to jump from a fully ordered state into a state with finite-domain size. Since it is reasonable to assume that a finite-domain-size configuration has negligible magnetization, we can intuitively understand the origin of the complete first-order phase transition observed with the CMFM.

The peculiarity of this transition and the relatively small variation of the internal energy in the disordered phase make it possible to obtain an estimate for the transition temperature by comparing the free energy of the FMFS configuration with the free energy of the disordered configuration. In order to compute the free energy of a disordered configuration, we use the average infinite-temperature internal energy of the system $E_{\infty} = JL^2$, an estimate derived via the CMFM in the preceding section and confirmed by the numerical results (see Sec. V). Then, we can use Baxter's exact result for the residual entropy as an estimate of the entropy and obtain the free energy of a disordered state at all temperatures:

$$F_{\text{disordered}} = JL^2 - T2L^2\ln(1.2087). \qquad (22)$$

By comparing the free energy of the FMFS state $F_{\text{FMFS}} = -3JL^2$ with $F_{\text{disordered}}$ we obtain an estimate for the tran-

sition temperature $2J/(\ln 1.2087) \simeq 10.55J$, which is reasonably close to the result from the CMFM $T_c \simeq 9.872J$.

IV. DEFECTS AND THEIR ROLE IN THE DYNAMICS

In this section we discuss the importance of defects in determining how the system can, dynamically, move from one of the allowed low-energy configurations to another. For concreteness, let us start by discussing the Josephson-junction arrays, i.e., the case of $\mathbb{Z}_2 \times U(1)$ symmetry.

A. Integer vortices

For finite U, it is best to understand the system in terms of the chirality Ising spins, plus XY spin waves of the $U(1)$ sector. The lowest-energy excitations over any configuration with Ising spins satisfying $\sigma_P^\bigcirc = \pm 6,0$ are topologically trivial (no vortices) XY spin waves.

When $\sigma_P^\bigcirc = \pm 6,0$ is preserved, vortices of the $U(1)$ sector can only have vorticity that is an integer multiple of 2π. These vortices cost an energy of order of magnitude U, the vortex core energy. The $U(1)$ phase twist leads to the usual logarithmic interaction between a vortex/antivortex pair,

$$\mathcal{E}_1 \propto U 2\pi \ln R. \tag{23}$$

and these pairs are confined below a Kosterlitz-Thouless-type transition at a temperature scale $T_{KT}^{(1)} \propto U$. Since we are interested in the regime of temperatures $T \ll U$ such that the three-color constraint is enforced, these integer vortices will be confined.

Now, what are the accessible excitations that break the $\sigma_P^\bigcirc = \pm 6,0$ constraint?

B. Fractional vortices

A fractional vortex excitation is illustrated in Fig. 7. Such fractional vortices are always created in pairs via a nearest-neighbor exchange of opposite pointing spins and they have been discussed by Park and Huse[12] in the case of the superconducting kagomé network. A fractional vortex excitation corresponds to a single hexagon that violates the $\sigma_P^\bigcirc = \pm 6,0$ constraint. We define its fractional vorticity as $\Gamma = 2\pi\nu = (2\pi/3)\sigma_P^\bigcirc \pmod{2\pi}$. Thus, we have $\nu = \pm 1/3$ for $\sigma_P^\bigcirc = \mp 2$ or $\sigma_P^\bigcirc = \pm 4$.

The presence of defects causes a fractional accumulation of the link sum of the vector potential $\vec{A}_{i,a}$, the equivalent of $\oint d\vec{\ell} \cdot \vec{A}$ in the continuum limit, that equals $\pm 2\pi/3$ $\pmod{2\pi}$. Once again it is useful to resort to the picture in Fig. 4 to understand that only one-third of the vorticity associated to an Ising spin at a vertex is included in the circulation around an elementary hexagon, and hence the flux is $\frac{1}{3} 2\pi\sigma_P^\bigcirc$.

To minimize the energy cost across the Josephson junctions, the superconducting phases θ_i in the triangles must adjust accordingly to pick this extra phase difference $\pm 2\pi/3$. Hence, an excited state that breaks the $\sigma_P^\bigcirc = \pm 6,0$ constraint in the Ising sector must be accompanied by a $U(1)$
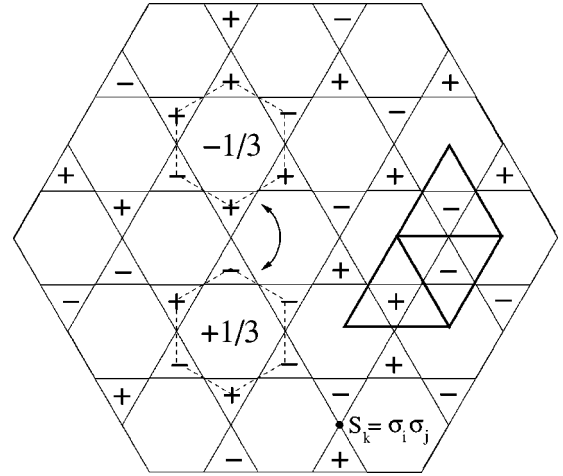

FIG. 7. A pair of $\pm 1/3$ vortices created by a nearest-neighbor spin exchange. The solid-line lattice represents the kagomé network considered by Park and Huse (Ref. 12). The Josephson-junction triangular array is represented instead by the bold triangles. The corresponding hexagonal lattice in our model is shown only around the two defects (dashed line). In the bottom right part of the picture we show the mapping to the bidual representation used in the CMFM.

phase twist that scales with the distance r from the defect as $1/(3r)$ (in units of the lattice spacing).

The $U(1)$ phase twist leads to a logarithmic interaction between a fractional vortex/antivortex pair a distance R apart:

$$\mathcal{E}_{1/3} \propto U \frac{2\pi}{3^2} \ln R. \tag{24}$$

Thermodynamically, there is an entropic contribution to the free energy, which was calculated by Moore and Lee,[9] and shown to also be logarithmic. Therefore, there is a confining transition of the Kosterlitz-Thouless-type at a temperature $T_{KT}^{(1/3)} \propto U/9$. If the Josephson coupling U is large compared to the temperature T, which is the regime we are interested in, then one is deep in the confined phase, and fractional vortices are rather ineffective as a source of phase-space reconfigurations.

C. Open segments of closed two-color loops

There is a special way to flip Ising spins along certain strings lying on the hexagonal lattice that, while violating the $\sigma_P^\bigcirc = \pm 6,0$ constraint, only costs energy at the extremities of the string, irrespective of its length.

To understand these excitations, let us start by looking at the simple case of a single spin flip that violates the constraint on three neighboring hexagons. In terms of the color model, all colors remain perfectly well defined, with the exception of the one vertex where the spin flip occurred. The energy cost of this defect is of order U. It is possible that locally adjusting the $U(1)$ phase near the defect might slightly relieve this cost, but we have not investigated this
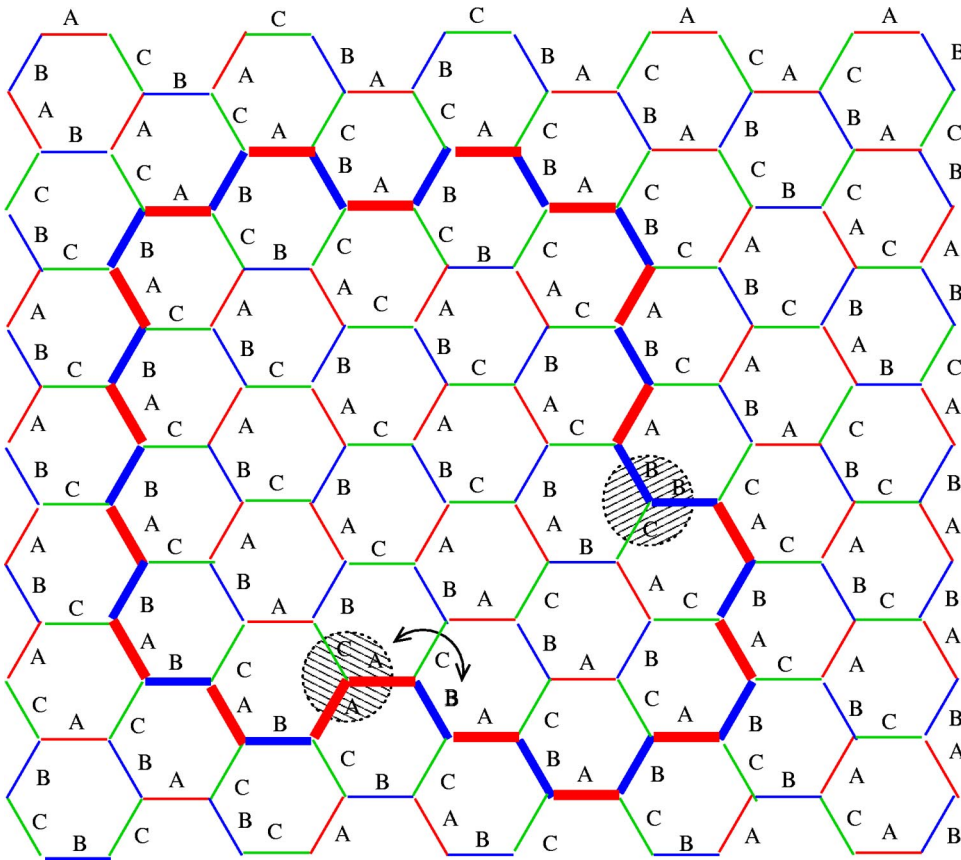
FIG. 8. (Color online) Defect pair at the end points of an open string, with end points highlighted (shaded circles) and the relative two-color path (bold links) shown in a configuration of the three-color representation of the model. The end points can travel freely along the path via nearest-neighbor color exchanges, such as the one outlined by the double arrow. Eventually, the two end points recombine by either exchanging all the bonds along the path or by leaving them all unchanged.

issue. A single spin flip could split into a $+1/3$ and $+2/3$ (or equivalently, a $-1/3$) fractional vortex pair. These, however, are confined together at low temperatures compared to U, as we argued above.

In the three-coloring model, this spin-flip defect corresponds to the initial step of creating an open segment defect described hereafter. Out of the three bonds departing from the spin-flipped site, two must have exchanged color (in order to change the chirality of the vertex), thus violating the color matching with the corresponding two neighboring sites. If we now move these two color defects starting from the two neighboring sites and performing the same original color exchange, we can propagate the defects at zero energy cost along a predefined path. Indeed, every color exchange will fix the previous color mismatch and create a new one, one lattice spacing apart. Notice that this process will flip all the spins between the two end points along the path. It is useful to recall the color description of the allowed low-energy states. Imagine one follows an ABAB . . . sequence that always forms a closed loop in an allowed configuration. We have already seen that flipping the whole loop to BABA . . . maintains the system in an allowed configuration. It is also trivial to show that this update flips all Ising spins visited by the loop. While this is a rather nonlocal move, starting from a single spin flip (color exchange) and propagating the color defects as above, we can realize this move through a sequence of local updates. Instead of flipping the whole loop at once, one can do it in steps, flipping the spins along a piece of the loop sequentially. Notice that the energy cost of this string is paid only at the end points

and is of order U, as long as the sequence of spin flips moves on its two-color track. The end points can be thought of as a defect pair connected by a string. This special path is hidden in the constrained Ising representation, but is clear in the three-color one (see Fig. 8). The defect pair, once formed, can diffuse around the one-dimensional loop, and it has two channels to decay back into an allowed state: either the defects recombine by going around the whole loop, leading to the BABA . . . configuration, or they recombine without winding around the loop back to the original ABAB . . . configuration. These are the defects considered by Kondev *et al.*[5] In the CFT description, they correspond to vertex operators with conformal dimension 1/2. While, as we mentioned, for a fixed configuration of colors there is no confining force between pairs, an effective interaction appears because of entropic reasons, producing an algebraic decay with the separation distance for the partition function in the presence of such defects. However, for the dynamics one is really interested in the cost for a given configuration. Therefore, the formation and recombination of these defect pairs constitute the main mechanism responsible for the dynamical evolution of the system.

The defect formation time just enters as an overall rescaling of the time steps for loop updates. Also, since the time it takes for the defects to move diffusively around the 1D loop is algebraic in the loop length (and not exponential), we can neglect this correction and simply treat the whole loop update as a nonlocal elementary move, now with a justified local origin.

V. DYNAMICS

In order to study the dynamic properties of the system, we use Monte Carlo (MC) simulation techniques of an $N = 2L^2$-site hexagonal lattice ($3L^2$ bonds) with periodic boundary conditions. As we discussed in Sec. II, the choice of the single-step update is nontrivial due to the color constraint. In Sec. IV we argued that the open segments of closed two-color loops are the main actors in the dynamical evolution of the system, based on energy and confineneck considerations. Thus, without loss of generality, we consider only loop updates as single-step updates of our MC technique. We also assume that the rate of formation of the open segment defects is low enough not to allow for defect proliferation (i.e., for the intersection of two different open segments before they recombine).

To implement a loop update we proceed as follows: we first choose one site and two colors at random; then we compute the energy difference in the system for the update of the corresponding loop; eventually we accept or reject the update based on the usual Boltzmann probability. Notice that, with this choice of the single MC step, the update of a loop takes one unit of time, independent of its length. In a possible experimental realization we expect the two ends of an open segment defect to walk randomly along the corresponding closed path, until they recombine. Thus, our MC dynamics is accelerated and the rescaling of our MC time with respect to a possible "real" time is highly nontrivial. Since we are interested in studying the slowing down and freezing of the dynamics in the three-coloring model, we choose to use the accelerated loop dynamics in order to be able to sample much longer time scales, otherwise inaccessible with a realistic update mechanism based on defect formation and recombination.

In terms of the loops, one can notice that the two ordered configurations FMFS and Néel (ferromagnetic and antiferromagnetic, respectively) correspond to the two extrema in loop curvature. In the FMFS configuration, the loops are completely straight loops, winding around the whole system. In the Néel configuration, the loops are maximally curved into single-hexagon loops. For these reasons, we expect an entropic jamming in the approach to the FMFS state, for a ferromagnetic choice ($J > 0$) of the interaction, as discussed in the case of infinite range interactions by Chakraborty et al.[4] Indeed, entropy favors rough and entangled loops, which in the infinite-temperature limit have a fractal dimension equal to 1.5.[5,18] This creates a phase-space bottleneck due to the small number of configurations that allow the system to reach the FMFS state with straight, packed loops. On the other hand, the approach to the Néel state in the antiferromagnetic interaction case ($J < 0$) is much smoother for the system. Even though this state has zero entropy by itself, single-hexagon flips allow the system to achieve a gain in entropy of the order of $\ln L^2$ with an energy cost of the order of $6J$. Indeed the Néel state corresponds to the *ideal states* defined by Kondev and Henley,[5] which have maximum entropy density in the sense that they allow for a maximum number of local rearrangements of the spins in accord with the constraint. Thus, we do not expect any jamming phenomena to play a role in this case.

In this section we consider only the case of ferromagnetic interactions and we set $J = 1$ as the unit of measure of energies and temperatures. In order to be able to access large simulation times, we choose the smallest system size for which our results do not show a significant dependence on system size ($L = 18$).

A. Transition temperatures

1. Estimate of the thermodynamic transition temperature

The first result that we observe both in cooling/heating simulations and in quenching simulations is the phase-space "isolation" of the single-crystal phase or FMFS. Even though at equilibrium the system must eventually favor the FMFS, we were unable to reach it within any simulation time, up to 10^7 MC steps. The system prefers to settle into a frozen polycrystalline (P-xtal) phase with zero or close to zero average magnetization, and with very slow, event-dominated dynamics. In Fig. 9 we show the time evolution of the system after a quench in temperature from $T \sim \infty$ to $T = 6.0$. After a single MC iteration [Fig. 9(a)], only a few small crystalline seeds are visible in a disordered liquid background. These seeds quickly develop into well-defined domains [Fig. 9(b)], whose size grows with time until the system becomes frozen into the P-xtal phase [Fig. 9(d)]. Notice the domain boundaries following the "crystalline planes" of the hexagonal lattice in the polycrystal. The dependence of the crystalline mass m on time t reflects the remarkable slowing down in the dynamics once the system enters the polycrystalline phase.

Even melting simulations starting from the FMFS phase and increasing the temperature are not useful to estimate the transition temperature. Indeed, they result in a large overestimate of T_c, since the melting time remains much larger than the simulation time well above T_c.

The only measure we can achieve of the thermodynamic transition temperature T_c is by computing the free energy in the liquid and crystal phases by integration of the internal energy. For a single crystal we know that $f_{\text{FMFS}} = -1$ at all temperatures, where $f = F/(3L^2)$ is the free energy per bond. For the liquid phase, we use the curves in Fig. 13 showing the dependence of the internal energy on the temperature. Notice that the asymptotic value of the internal energy at infinite temperature is different than zero. This is purely due to the constraint, which appears to be slightly antiferromagnetic in nature. A simple way to visualize this effect is to look at an infinite-temperature configuration after performing a spin-flip operation on one of the two sublattices of the hexagonal lattice. The result is shown in Fig. 10.

An appropriate fit of the common high-temperature region of the internal energy (per bond) curves,[19]

$$\mathcal{E}_{\text{liquid}}(T) = c - a/T^b \tag{25}$$

gives $a \simeq 4.3$, $b \simeq 1.22$, and $c \simeq 0.336$. Notice that a naive high-temperature expansion in powers of $1/T$ may be plagued by the criticality at high temperatures. In this sense
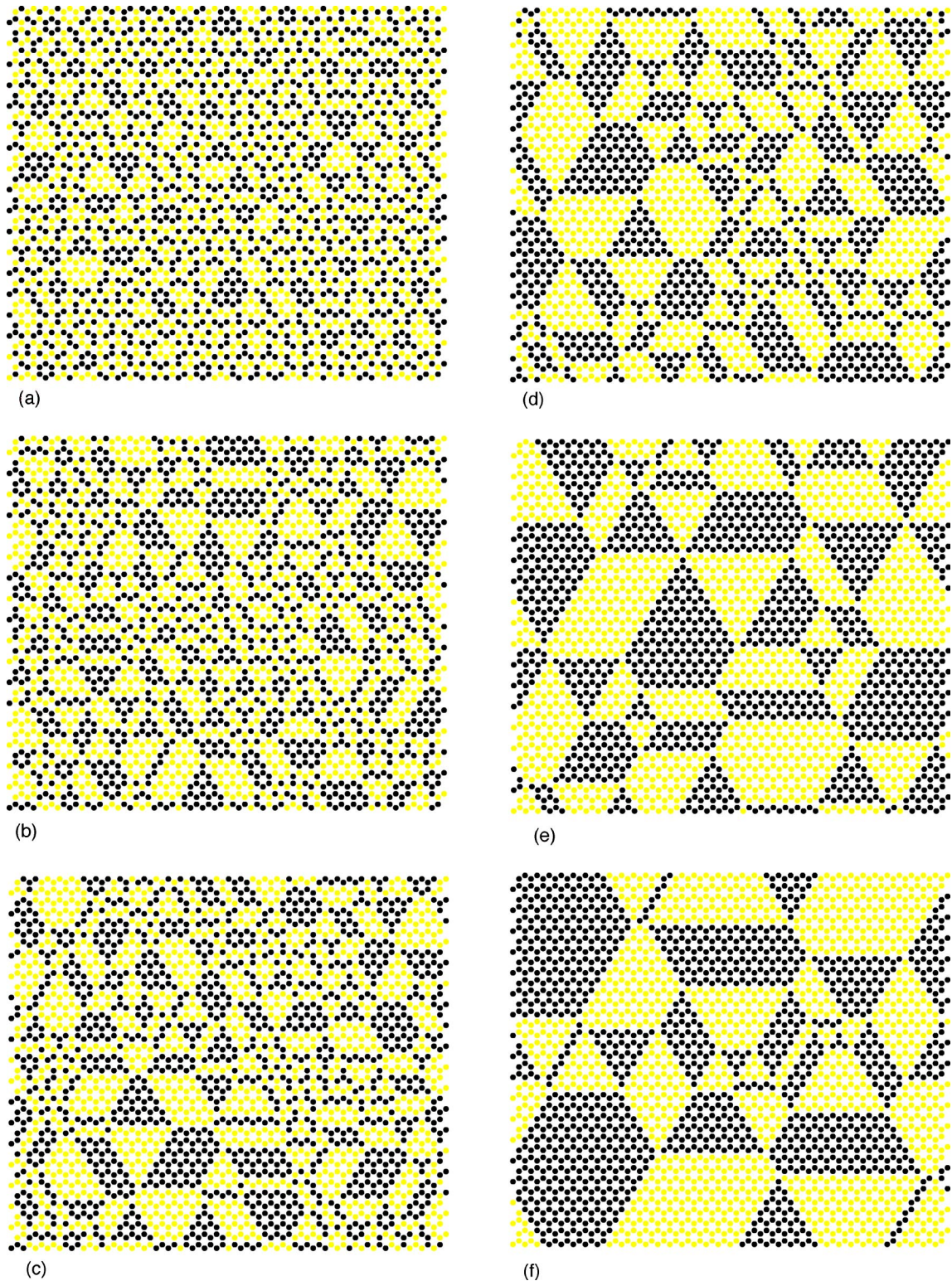
FIG. 9. (Color online) Time evolution snapshots of the system after a quench from $T \sim \infty$ to $T = 6.0$ (at time $t = 0$) below the transition temperature $T^* \simeq 8.1$. The dots represent the $2L^2$ vertices of the hexagonal lattice ($L = 36$) and the two colors correspond to the two values of the chirality spin. The lattice is wrapped along the horizontal axis and along the 60° axis rotated counterclockwise above the horizontal. For each configuration, we report the measured crystalline mass m and the time t from the temperature quench: (a) $m = 0.08$, $t = 1$ MC step; (b) $m = 0.24$, $t = 28$ MC steps; (c) $m = 0.32$, $t = 49$ MC steps; (d) $m = 0.50$, $t = 192$ MC steps; (e) $m = 0.68$, $t = 5.7 \times 10^4$ MC steps; and (f) $m = 0.73$, $t = 5.4 \times 10^5$ MC steps.
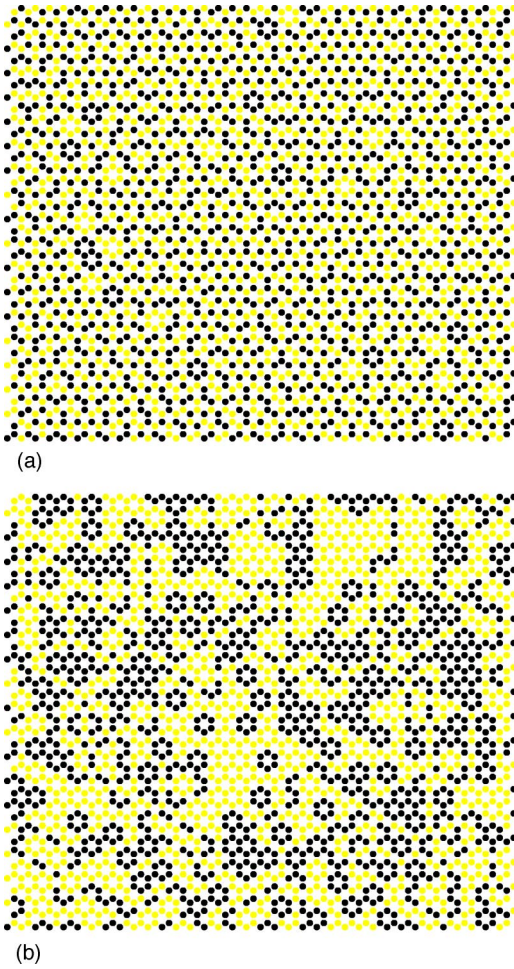
FIG. 10. (Color online) Two pictures of an $L=36$ system configuration at infinite temperature: (a) the original chirality spins; (b) the same configuration after we performed a spin-flip operation on one of the two sublattices. The antiferromagnetic correlations originating solely from the constraint are clearly visible.

the nontrivial exponent b may have an interpretation in terms of the CFT description at $T \to \infty$. We can then integrate to obtain the free energy:

$$\beta f(\beta) = \beta_0 f(\beta_0) + \int_{\beta_0}^{\beta} d\beta' \mathcal{E}(\beta'); \qquad (26)$$

setting $\beta_0 = 0$ for the liquid phase and using the known residual entropy of the system, we obtain

$$f_{\text{liquid}}(T) = -\frac{2}{3}\ln(1.2087)T + c - \frac{a}{(b+1)T^b}, \qquad (27)$$

where the 2/3 factor in front of the residual entropy comes from the fact that there are three bonds every two spins. Setting $f_{\text{liquid}}(T) = f_{\text{FMFS}} = -1$ gives the melting temperature $T_c = 9.6$, in good agreement with the results from the CMF method.

Even though T_c is the actual thermodynamic transition temperature, we are unable to observe this transition due to the incredibly large time scales involved in the approach to

the FMFS state. As it appears from the results below, the system seems to be completely unable to sample the phase-space region corresponding to the crystalline phase, at least on our simulation time scales, and it is confined to an "effective phase space."

2. The dynamic freezing transition

Instead of going through the thermodynamic transition, the system remains in a supercooled liquid state below T_c, until it reaches a temperature T^* where it evolves into a frozen polycrystalline state.

Looking at Fig. 9(f), we can clearly see that the polycrystallization is complete, in the sense that the domain boundaries are fully one dimensional, with almost no interstitial liquid left. While the size of these domains increases with longer waiting times, the growth becomes extremely slow, basically stopped within our Monte Carlo time scales before reaching the single-crystal configuration. This can be observed, for example, in the behavior of the zero-temperature saturation value of the energy in Figs. 13 and 14. The energy is in fact a measure of the area-to-perimeter ratio in the polycrystalline phase, provided complete polycrystallization has been achieved. This is clearly the case in the $T \to 0$ plateaus in Fig. 13. Instead of approaching the value -1, characteristic of the FMFS state, these plateaux seem to approach a limiting value $\mathcal{E}^{\text{P-xtal}}(T=0) \sim -0.74$ for larger cooling times.

The transition at T^* can be seen as a dynamic phase transition and does not have a thermodynamic origin. However, we can reasonably establish a correspondence of this transition to a "true" thermodynamic phase transition in a related, more constrained system. As we show with the following analysis, the origin of the dynamic transition at T^* resides in a free-energy barrier that prevents the system from visiting a phase-space region around the FMFS phase, at least within our simulation time scales. Since only winding loop updates can change the number of bonds per color per direction, it is possible to divide the phase space into topologically separated sectors by forbidding the update of winding loops. The FMFS configuration would then be in a topological sector by itself, and starting from an infinite-temperature configuration with equal number of bonds per color per direction it would be impossible for the system to reach its natural ground state. With this constraint, the system is expected to show a phase transition into a state which is not the FMFS, with a behavior analogous to the one observed in the present model.

This polycrystal transition is an intrinsic transition of the supercooled liquid phase, which would not exist in the infinite time limit. If we were able to wait infinite simulation times, we expect the dynamic transition at T^* to disappear, replaced by the equilibrium transition at $T_c > T^*$.

Since we cannot apply the same technique used above for T_c to the polycrystalline state, we have to measure T^* with a somehow more empirical method. We first prepare the system into an almost completely polycrystallized state by cooling it at very low rates. We then chose a particular value for the temperature T and let it evolve in time. If it eventually reaches the liquid state, then we conclude that $T > T^*$; conversely if it completes the polycrystallization process. The
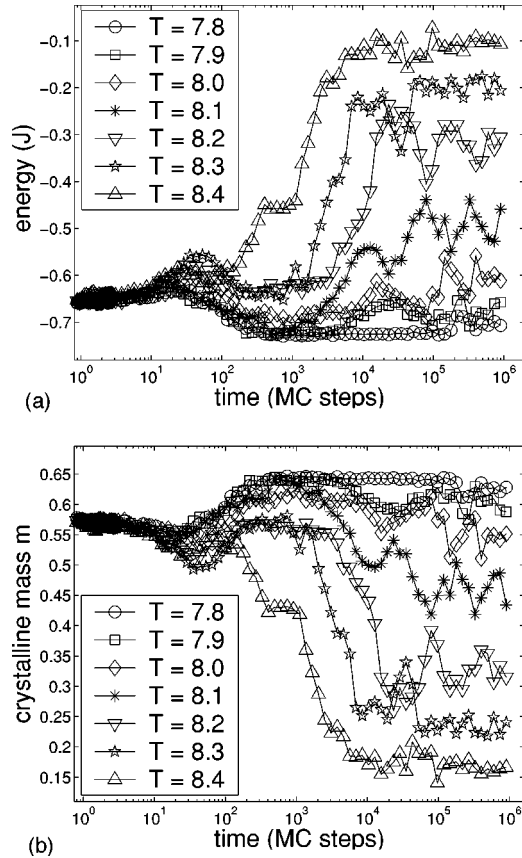
FIG. 11. Time evolution of the internal energy and crystalline mass, after the system has been prepared in an almost polycrystallized configuration. The curves correspond to different quenching temperatures (expressed in units of J) both above and below the transition temperature $T^* \simeq 8.1 \pm 0.1$. Note that all the temperatures are below the thermodynamic transition temperature $T_c \simeq 9.6$, while the system behaves as if it is incapable of visiting the favored FMFS configuration.

choice of the initial state closer to the polycrystalline state rather than to the liquid one is merely due to the stronger metastability of the liquid phase, as it appears from the asymmetry in the hysteretic process with respect to T^* [see Fig. 13(a)]. In Fig. 11 (top) we present the results in terms of time evolution of the energy. Even though we do not have a sharp distinction between the behavior above and below T^*, we can clearly identify a transition at $T^* \simeq 8.1 \pm 0.1$. When the system is set to a temperature $T > 8.2$, it quickly departs from the quasipolycrystallized initial state, while for $T < 8.0$ it completes the polycrystallization process, thus lowering its energy. It is interesting to notice that all the quenching temperatures are below the thermodynamic transition temperature $T_c = 9.6$, while the system behaves as if it is incapable of visiting the favored FMFS configuration.

Since the total magnetization of the system remains close to zero for all temperatures and time scales that we are able to sample, it cannot be used as an order parameter for this transition. A more appropriate order parameter is probably the crystalline mass m, shown in Fig. 11 (bottom). As proposed by Cavagna et al.,[20] the crystalline mass measures the fraction of crystallized spins independently of the size of the

polycrystals. We first define the elementary crystal unit as the four-spin cluster composed of one spin and its three nearest neighbors. To avoid double counting, we choose the central spin exclusively in one of the two sublattices of the hexagonal lattice. Then, we define the (dimensionless) crystal mass density $m \in [0,1]$ as the number of these elementary units present in a given configuration, normalized by the total number of units L^2. Since we need to keep the elementary unit small enough to be sensitive to small amounts of crystal mass, we have a limited power of resolution. In fact, even a random configuration has a nonzero average crystalline mass $m_0 = 0.01$, which we consider as the effective zero of m. The results obtained by measuring the time evolution of m are in good agreement with the conclusion that $T^* \simeq 8.1 \pm 0.1$.

3. Some considerations on the dynamics of the polycrystal

The data shown in Fig. 11 are averages over 32 different histories starting from the same initial configuration. The reasons for the large time fluctuations and the lack of a sharp distinction between above-T^* and below-T^* behavior, as shown instead in the system studied by Cavagna et al.,[20] are to be found in the peculiar, rare-event-dominated dynamics of the polycrystalline phase. It is worth to analyze this dynamics in detail, as it helps understanding also the phase-space isolation of the thermodynamic g.s., i.e., the FMFS crystal.

With some simple reasoning about the colors and the chirality spins, one can see that within a single, ferromagnetically ordered domain, all the bonds of the same color are aligned in the same direction. Thus, any two-color sequence inside the domain follows a straight path from one side to the other along one of the three crystalline directions (or crystalline planes) of the hexagonal lattice. This high level of order is responsible for the first important difference with respect to usual domain growth: there are no small loops across the boundary of a domain (but for possible corner loops) and the domain is not capable of small rearrangements of its walls. While, for example, in a normal Ising model a domain can expand gradually, in our constrained Ising model a domain can only crack from side to side. It is important to notice that these cracks will almost always bring the system into an excited state with higher energy, the energy difference being proportional to the length of the crack.

If we now extend these considerations to the almost complete polycrystalline phase that the system is able to achieve below T^* (see Fig. 9), we can see that any loop has to cross a few domains before closing on itself. In fact, bending of the loops are allowed only at domain boundaries. Therefore, we have a second important difference with respect to usual domain growth: one domain cannot expand at the expenses of a single other domain; rather, the above cracks involve at least six domains (but for the case of winding loops), since every domain boundary corresponds to a 60° bending in the loop. One can easily convince oneself that the closer the system is to the polycrystalline phase, the more the dynamics become frozen, requiring entangled, multiple-domain cracking in order to move from one configuration to another. This behavior can be seen, for example, by looking at the behavior of the spin-spin autocorrelation function [see Eq. (29)],
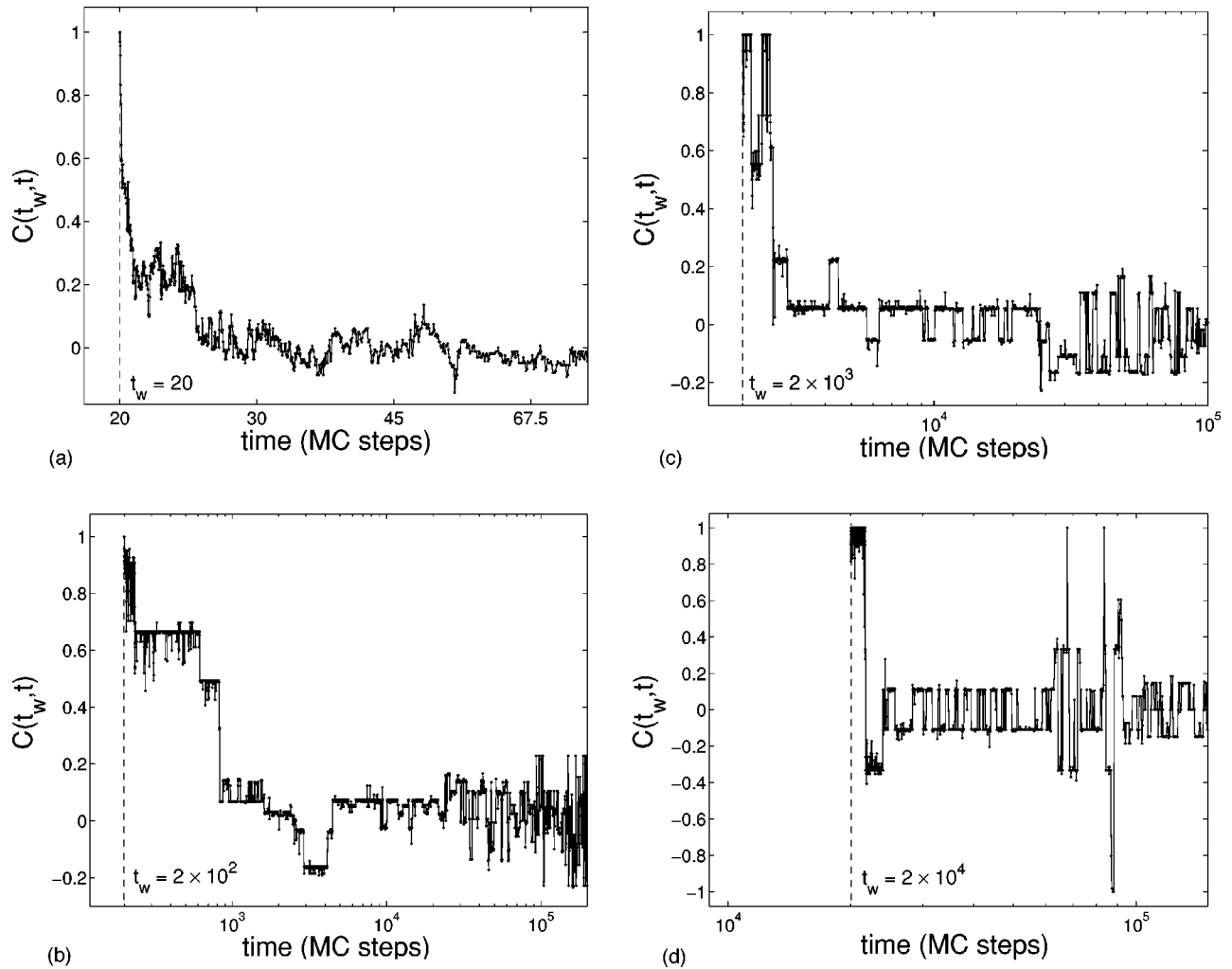
FIG. 12. Spin-spin autocorrelation function $\mathcal{C}(t_w,t)$ for a single MC simulation and four different values of the waiting time t_w: (a) $t_w=20$ MC steps; (b) $t_w=2\times10^2$ MC steps. Note the rescaling of the time axis with respect to the previous figure; (c) $t_w=2\times10^3$ MC steps; and (d) $t_w=2\times10^4$ MC steps. The temperature is quenched at $t=0$ from $T=\infty$ to $T=6$, the same used in Fig. 9. At $t_w=20$, the system is still in a rapidly changing liquid phase [see Fig. 9(b)]. As the system gets deeper into the polycrystalline phase at $t_w=2\times10^3$ or even more at $t_w=2\times10^4$ [see Fig. 9(d)], the behavior of the correlation function becomes discontinuous, reflecting a rare-event dominated dynamics where the system undergoes highly nonlocal rearrangements. Notice the $\mathbb{Z}_2$ symmetry of the system [Fig. 12(c)]. When the dynamics become highly entangled in the polycrystalline phase [see Fig. 9(e)], the number of allowed configurations drops dramatically and rearrangements that bring the system from one configuration to its mirror image play a significant role in the evolution of the system.

shown in Fig. 12. For small values of t_w, the system is still in a rapidly changing liquid phase [see Fig. 9(b)], and the correlation function roughly follows the stretched exponential behavior with a very short relaxation time discussed in Sec. V B 2. As the system gets deeper into the polycrystalline phase for $t_w=2\times10^3$ or even more for $t_w=2\times10^4$ [see Fig. 9(d)], the behavior of the correlation function shows how the system now evolves mostly via rare events that are responsible of extended changes in the system configuration. Notice the $\mathbb{Z}_2$ symmetry of the system. When the dynamics become highly entangled in the polycrystalline phase [see Fig. 9(e)], the number of allowed configurations drops dramatically and rearrangements that bring the system from one configuration to its mirror image play a significant role in the evolution of the system [Fig. 12(c)].

It is important to underline the large energy cost of these updates, which scale with the linear size ξ of the domains.

Indeed, we can interpret this energy difference as the activation energy $E_A(\xi)$ for domain growth. Processes where the activation energy depends on ξ, or more generally where freezing involves a collective behavior dependent on ξ belong to classes 3 and 4 for growth kinetics.[21] In the following paragraph, we will address this classification in greater detail.

Even if the system is able to overcome the activation energy barrier, the three-coloring constraint plays a new key role in preventing the system from reaching a new configuration. Let us consider an excited state after one loop has been updated in the polycrystalline phase. The system has then three types of updates available: the trivial repair of the crack, with consequent lowering of the energy; an independent update, which requires to overcome a similar activation energy; and the peculiar loop updates that are adjacent to the open crack. Clearly, since a loop update corresponds to flip-

ping all the spins along the loop, the latter update has a vanishing energy cost because the original crack crosses crystalline ordered domains. Thus, the system is able, via these adjacent loops, to expand or contract a crack with essentially equal probability. Indeed we expect this process to be similar in nature to a random walk, with two possible outcomes: the crack eventually contracts and closes on itself, or all the domains involved in the original crack get essentially flipped, with minimal structural change in the original configuration. Notice that the last update in this process is of the repair type, with the system getting back to a lower-energy state. The time to complete this process is the lifetime τ_d of a crack in the system, while the formation time of a new crack is determined by the activation energy barrier $\tau_f \sim \exp[-\beta E_A(\xi)]$. At low temperatures, τ_d is much shorter than τ_f; the system freezes into a specific polycrystalline configuration and the dynamics involve only rare events where entire domains are flipped simultaneously. At temperatures close to T^* instead, τ_d becomes comparable to τ_f and multiple cracks allow the system to deeply rearrange the domains. Notice, however, that it is still a rare-event dependent dynamics. In a typical process of configuration change, the system visits highly excited states with complete ``melting'' of extended areas of the polycrystal, before freezing again into a new polycrystalline configuration . These highly excited intermediary states easily become long lived due to the metastability of the liquid phase, which has instead very fast dynamics (see Fig. 15 and the results hereafter).

B. One-time quantities

1. Energy vs temperature and growth dynamics

In order to get a better insight in the dynamics of the model, we study the behavior of the system through temperature hysteresis with different cooling/heating rates. We vary the temperature from $T=40$, where the liquid phase is stable and equilibrates very easily, down to $T=0$ and up again to $T=40$, with a constant rate given by $r=\Delta T/\Delta t$, Δt being the total time to go from $T=40$ to $T=0$. During these simulations we measure all the relevant quantities in our system: the internal energy, the magnetization, the staggered magnetization, and the crystalline mass. Both magnetizations remain close to zero for any temperature and cooling/heating rate. The behavior of the internal energy is shown in Fig. 13 for some of the cooling/heating rates that we consider. The behavior of the crystalline mass is in agreement with the internal energy and does not provide any additional information.

The hysteresis observed in the energy curves is typical of first-order phase transitions. From Fig. 13 we can see that the hysteresis gets narrower for smaller values of r, indicating a transition temperature that is consistent with our previous estimate $T^* \simeq 8.1 \pm 0.1$ (that estimate is also confirmed by looking at the position of the peaks in the specific heat, measured from the energy fluctuations, for different cooling/heating rates). Notice the asymmetry of the hysteresis toward the liquid phase, particularly evident for large cooling/heating rates, due to the metastability of the liquid with respect to the polycrystalline phase. For large cooling rates,
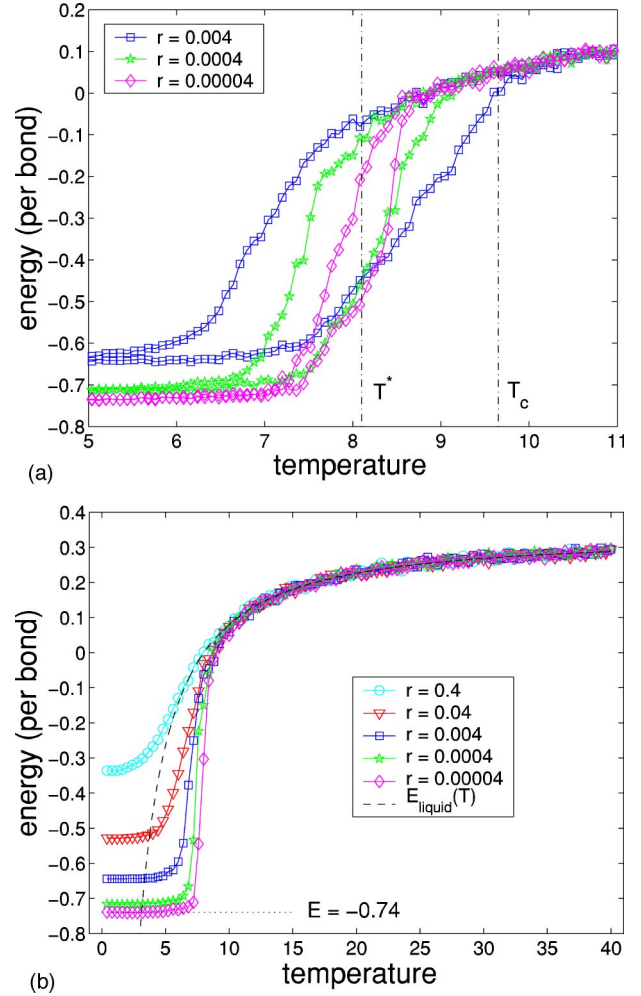

FIG. 13. (Color online) Internal energy vs temperature behavior for our system, in the temperature range $T \in (0,40)$: (a) temperature hysteresis for three different values of the cooling/heating rate: $r = 0.04$, 0.004, and 0.00004. The hysteretic behavior is typical of a first-order phase transition and it is in good agreement with our measure of T^*; (b) cooling curves for five different cooling rates: $r = 0.4$, 0.04, 0.004, 0.0004 and 0.00004. The dashed line is the extrapolated internal energy of the liquid phase [Eq. (25)]. Notice that, for $r = 0.4$, the system stays in the liquid phase until $T=0$, since the energy curve remains above the dashed line at any temperature (Ref. 20). Energy and temperatures are in units of J, while the cooling/heating rates are expressed in units of J/MC step. These curves are obtained from simulations where the temperature is changed at a constant cooling/heating rate. For large temperatures ($T > 15$), all the curves overlap and the system is at equilibrium in the liquid phase. Notice that there is no sign of the thermodynamic transition at $T_c = 9.6$, as the system goes smoothly into the supercooled liquid phase.

see, for example, $r = 0.4$ in Fig. 13, the energy curves never cross below the extrapolated $\mathcal{E}_{\text{liquid}}(T)$ curve (dashed line in the figure). Thus,[20] the system does not polycrystallize and it remains in a supercooled liquid phase with respect to the polycrystalline phase until $T=0$ (recall that the liquid is already supercooled with respect to the FMFS phase for $T < 9.6$). This is confirmed also by the absence of a peak in the specific-heat curves. As the temperature is lowered to zero,
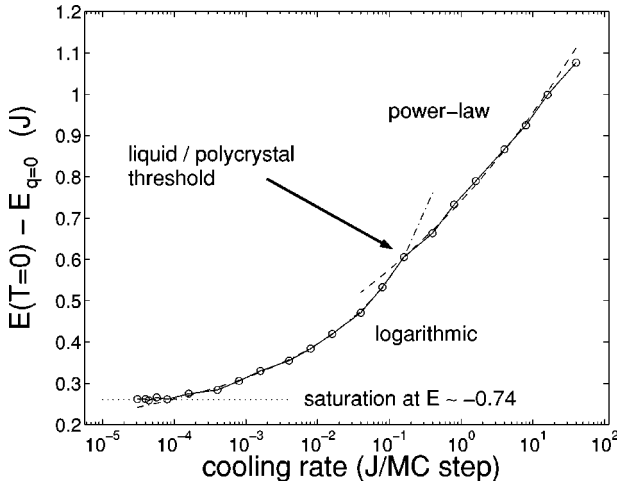
FIG. 14. Semilogarithmic plot of the plateau value of the internal energy with respect to the g.s. energy of the perfect crystal ($\mathcal{E}_{\text{FMFS}} = -1$) vs the cooling rate $r = \Delta T/\Delta t$. Three distinct behaviors can be identified: a power-law behavior $\mathcal{E} \sim r^{0.11}$ for $r > 0.2$, when the system remains in the liquid phase; a logarithmic behavior $\mathcal{E}^{-1} \sim \ln(1/r^{0.85})$ for $8 \times 10^{-5} \leq r \leq 0.2$; and a saturation plateau at $\mathcal{E}^{\text{P-xtal}}(T=0) \sim -0.74$ for $r < 8 \times 10^{-5}$.

the curves reach a final value of the energy that decreases monotonically with smaller cooling rates. But for very large values of r (larger than 0.4), this final value of the energy is reached already at a finite temperature and the curves show a plateau typical of frozen or very slow dynamics. While we expect this behavior when the system enters the polycrystalline phase, we can notice that this plateau is also present for curves where the system remains in the supercooled liquid phase [e.g., see the curve for $r = 0.4$ in Fig. 13]. A detailed analysis of this behavior is beyond the scope of the present paper and will be addressed in the future.

The dependence of the $T = 0$ value of the energy on the cooling rate reflects the type of domain growth in the system. In particular, when the system enters the polycrystalline phase where domain boundaries are one dimensional, the energy difference $\mathcal{E}(T=0) - \mathcal{E}_{\text{FMFS}} = \mathcal{E}(T=0) + 1$ is proportional to the inverse of the linear size of the domains.[20] In Fig. 14 we show the behavior of $\mathcal{E}(T=0) - \mathcal{E}_{\text{FMFS}}$ as a function of r.

As long as the system remains in the liquid phase, i.e., the energy curves never cross below the extrapolated $\mathcal{E}_{\text{liquid}}(T)$ curve, the energy follows a power-law dependence on r: $\mathcal{E} - \mathcal{E}_{\text{FMFS}} \sim r^{0.11}$. This is typical of class 1 growth kinetics, where freezing originates from local defects with activation energies independent of the domain size ξ.[20,21]

As we lower the cooling rate, we reach a threshold where the energy curves start crossing the extrapolated $\mathcal{E}_{\text{liquid}}(T)$ curve and the system polycrystallizes. This threshold happens at $r_{\text{th}} \simeq 0.2$ and $\mathcal{E}_{\text{th}} \simeq -0.39$. Below this threshold, the behavior of the energy changes abruptly into a logarithmic form:

$$\mathcal{E}(T=0) - \mathcal{E}_{\text{FMFS}} = \frac{1}{1 + A\left[\ln\left(\dfrac{1}{r\tau_1}\right)\right]^m}. \tag{28}$$

From a fit of the results we obtain $m \simeq 0.85$, even though our numerical data do not have enough accuracy to exclude the case $m = 1$. If our measurement of $m \neq 1$ is confirmed, it implies that the behavior of our system for $r \in [8 \times 10^{-5}, 0.2]$ belongs to class 4 growth kinetics.[21] Both class 3 (corresponding to the case of $m = 1$) and class 4 kinetics are typical of processes that involve a ξ-dependent collective behavior in the frozen phase. As discussed above, we indeed expected the system to show this logarithmic behavior.

Eventually, for $r < 8 \times 10^{-5}$ the energy saturates to a limiting value $\mathcal{E}^{\text{P-xtal}}(T=0) \sim -0.74$, in agreement with the entropic argument we provided before. The system behaves as if a whole region of phase space around the FMFS configuration is dynamically inaccessible due to a very large free-energy barrier.

To further confirm this peculiar free-energy landscape, we use again the CMFM described in Sec. III C. From the numerical results, we assume as a first-order approximation that the dynamically excluded configurations correspond to system energies smaller than the limiting value $\mathcal{E}^{\text{P-xtal}}(T=0) \sim -0.74$. We then impose appropriate constraints on the variational parameter such that the only allowed energies in the CMFM are larger than $\mathcal{E}^{\text{P-xtal}}(T=0)$. Under these constraints, the method predicts a first-order phase transition at $T^* \simeq 8.36$, in good agreement with the numerical value $T^* \simeq 8.1 \pm 0.1$, considering the approximations underlying this CMFM result.

2. Domain nucleation vs liquid relaxation

Here we study the equilibration time of the liquid phase in comparison to the nucleation time for the polycrystalline phase.

We measure the connected piece of the two-times autocorrelation function

$$\mathcal{C}(t_w, t) = \frac{1}{2L^2} \sum_i \langle \sigma_i(t_w)\sigma_i(t) \rangle, \tag{29}$$

where $\langle \cdots \rangle$ indicates the average over initial configurations of different MC simulations. Notice that $\Sigma_i \sigma_i(t) \simeq 0$ for all values of t within our simulation time scale, thus the disconnected piece of the autocorrelation function vanishes. Since we are interested in the relaxation time of the liquid phase at equilibrium, we quench the system from infinite temperature down to the target temperature T and we wait for it to equilibrate. The correlation function becomes time-translation invariant and depends only on the time difference $t - t_w$. At equilibrium, we adequately fit $\mathcal{C}(t - t_w)$ with a stretched exponential, which is the expected equilibrium behavior in supercooled liquids:[20]

$$\mathcal{C}(t) = \exp[-(t/\tau)^\beta]. \tag{30}$$

From the fit we obtain the relaxation time τ as a function of the quenching temperature, as shown in Fig. 15. We can extend the measurement of τ below T^* because of the metastability of the liquid phase. The system is able to equilibrate as a supercooled liquid well before the polycrystal transition takes place, at least for temperatures close enough to T^*.
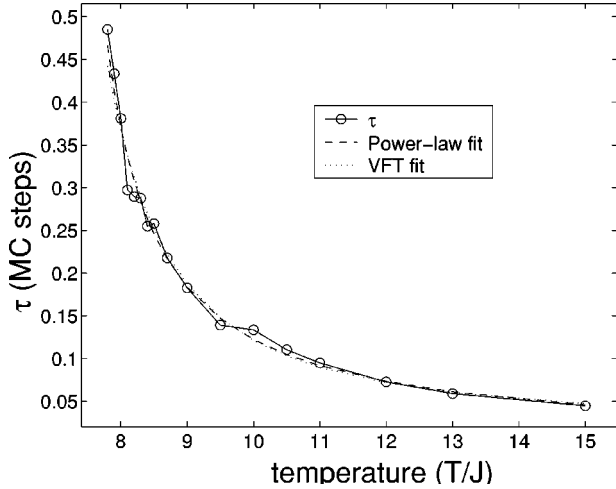
FIG. 15. Liquid phase relaxation time τ as a function of temperature, as measured from the stretched exponential fit of the autocorrelation function at equilibrium. The dashed line corresponds to a power-law fit while the dotted line corresponds to a Vogel-Fulcher-Tamman fit. Notice that there is no dynamic signature of the transition at temperature T^*.

FIG. 16. Time evolution of the energy of the system, after a quench from infinite temperature down to a target temperature T = 5.5, 6.0, 6.5, 7.0, 7.5, 8.0, and 8.5 (both energy and temperature are measured in units of J). The horizontal line corresponds to the energy threshold for polycrystallization $\mathcal{E}_{th} \simeq -0.39$, as identified above.

Notice that there is no dynamic signature of the polycrystal transition at T^* in the liquid relaxation time. The Kohlrausch exponent β of the stretched exponential fit decreases with temperature, as for realistic models of liquids. In Fig. 15 we show the fit of the τ data both with a power law,

$$\tau = \frac{A}{(T-T_c^{lq})^\gamma}, \quad T_c^{lq} = 7.0, \quad \gamma = 1.0, \quad (31)$$

and with a Vogel-Fulcher-Tamman (VFT) form,

$$\tau = \tau_0 \exp\left(\frac{\Delta}{T-T_0}\right), \quad T_0 = 4.4, \quad \Delta = 11.1. \quad (32)$$

The results of these fits have to be considered with extreme care. Because of the accelerated nonlocal dynamics and because of the onset of polycrystal nucleation, the temperature range where we are able to measure the relaxation time of the liquid phase allows for τ to vary only over a narrow interval, from 0.05 to 0.5 MC steps. As a consequence, the values obtained for the fitting parameters lack in accuracy, since the fit spans a single decade of data. Moreover, a VFT behavior typically involves the large τ limit of the $\tau(T)$ curve, which is not accessible in the present system due to the rapid nucleation of the polycrystal. Indeed, our numerical data are the tail of a possible VFT behavior, and they suggest that a VFT behavior may be observed in the liquid phase of this system if the polycrystallization process were to be avoided.

Since the correlation function decays to zero in $\approx 20\tau$, we can take this value as the equilibration time for the liquid phase at a given temperature:[20] $\tau_{eq}(T) = 20\ \tau(T)$.

Measuring the nucleation time of the polycrystalline phase in this system is instead more complicated. Due to the frozen nature of the polycrystalline phase, we cannot compute its free energy as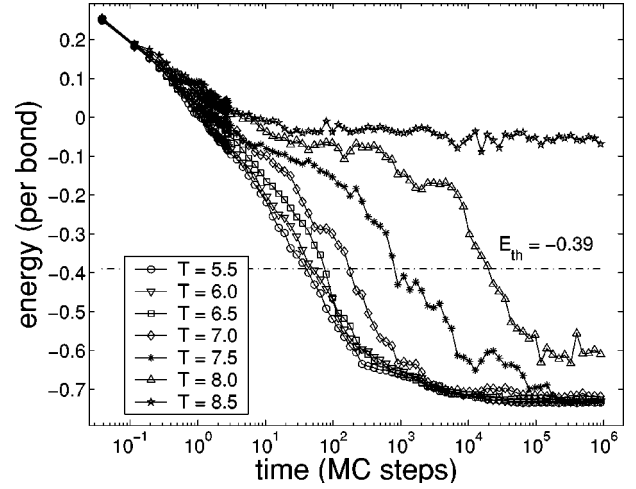 a function of temperature as we did for the liquid phase (see Sec. V A 1). Thus, methods such as the one in Cavagna *et al.*[20] are not applicable. More naively, we have to estimate τ_{nucl} directly observing the time evolution of the system. In Fig. 16 we plot the energy dependence on time for quenches of the system from infinite temperature to the target temperature T. As we discussed above, the system polycrystallizes when the energy falls below a threshold value $E_{th} \simeq -0.39$. Here we use this value in order to identify the onset of the polycrystallization process in the energy curves in Fig. 16. The time when the system starts developing a polycrystalline phase is indeed the nucleation time τ_{nucl} we are interested in. We can see that $\tau_{nucl} \simeq 800$ at $T = 7.5$ while it drops to $\tau_{nucl} \simeq 170$ at $T = 7.0$.

Comparing these results with the ones of Fig. 15, provided we perform the rescaling $\tau_{eq} = 20\ \tau$, we can see that the crossover $\tau_{eq} = \tau_{nucl}$ will happen at a temperature T_{sp} close to T_c^{lq}, where the liquid relaxation time shows a rapid growth. We can reasonably locate this crossover in the temperature range $7.0 < T_{sp} < 7.5$. This temperature is the spinodal temperature corresponding to the metastability limit of the liquid, when the liquid equilibration time scales become of the same order of the nucleation time scales and the liquid phase becomes unstable. The system reaches this limit in a time t_{sp} of the order of a few hundred MC steps.

VI. CONCLUSIONS

In this paper we have studied the very interesting properties of a model for describing the behavior, both static and dynamic, of different arrays of superconducting devices. Among the examples discussed, the main candidate to see such a rich phenomenology is a Josephson-junction array of triangular grains of superconductors with $p_x \pm ip_y$ order parameter. In the limit of very strong Josephson couplings, the system is equivalent to Baxter's three-color model in the hexagonal lattice. This model can in turn be represented by

an Ising model with a constraint on the total magnetization for each hexagonal plaquette, $\sigma_P^\bigcirc = \pm 6, 0$. In this paper we have presented a proof of this mapping based on the condition of the single valuedness of a superconducting order parameter. The Ising degrees of freedom correspond, in the Josephson arrays with p-wave islands, to the chirality of the $p_x \pm i p_y$ order parameter.

Within the constrained $\sigma_P^\bigcirc = \pm 6, 0$ space, the system is critical at infinite temperature but orders at any finite temperature if antiferromagnetic interactions between the Ising spins are present. For ferromagnetic interactions, it remains critical until a very particular first-order phase transition takes place, where the system orders completely. This behavior is due to the peculiar nature of the ordered state, which is isolated in phase space from any of its excitations by an energy of the order of the system size.

For a finite Josephson coupling strength, defects are present in the system, and there are violations of the color and, consequently, $\sigma_P^\bigcirc = \pm 6, 0$ plaquette constraint. A particularly interesting kind of defect is a fractional vortex pair. Within the context of the Josephson array of $p_x \pm i p_y$ superconducting islands, not only there is a large energetic cost to create these excitations, but they are also confined at low temperatures by logarithmic interactions. The other kind of interesting excitation is formed by flipping the spins along open segments of closed two-color loops. While there is also an energetic cost to create them, these defects can circulate on the lattice without further energetic cost, in contrast with the fractional vortices. Moreover, a new defect-free color configuration is obtained through the process of creation of a string of spin-flip excitations, the propagation of the defect along the two-color loop, and the recombination of the ends of the string after closing the loop. This mechanism is precisely the microscopic origin of the Monte Carlo dynamics that we implement in this paper.

Because of the constraint, the dynamics of the system is very peculiar. While the existence of a supercooled liquid phase is typical of first-order transitions, for our constrained system we find a whole temperature range in which such supercooled liquid is stable for extremely long time scales. Indeed, at all the time scales studied in this paper, the fully order phase cannot be reached and the system orders into a polycrystalline phase in which the global $\mathbb{Z}_2$ symmetry is unbroken. The transition from the liquid state to the polycrystal takes place at a critical temperature T^*, smaller than the static (avoided) critical temperature. This dynamical temperature T^* has been obtained both by studying the time evolution of the system after preparing it in a polycrystalline configuration, and by quenching the system from the liquid phase. The values obtained for T^* are in agreement with the naive estimate that we are able to obtain from the CMFM technique. The numerical analysis of the nucleation time and the liquid phase relaxation time allows us to give an estimate of the spinodal temperature of the liquid.

The rich phenomenology of the dynamics of this system is also reflected in the dependence of the difference between the final internal energy reached by the system and that of the fully ordered state on the cooling rate. While for very fast cooling rates this dependence shows a typical power-law scaling, the nucleation of the polycrystalline phase produces a logarithmic behavior until a total arrest in the domain growth is reached, meaning probably another logarithmic growth but with a much longer time scale. The origin of this scenario is the fact that the energy barriers through which the system has to pass to reach states with larger clusters grow with the size of the clusters. This places our system as one of the rare cases without randomness in which the dynamics is of class 3 or 4 in the classification of Lai et al.[21]

An important open problem concerns the possible mechanism to get out of the polycrystalline state. Proliferation of other (confined) type defects, such as fractional vortices, is a possible mechanism to help overcome the totally arrested dynamics in the polycrystalline phase. In this case, the large time-scale dynamics could be governed by the energetic cost of making a rather rare-event dominated proliferation and circulation of such (confined) defects. It is noteworthy that, in the polycrystalline phase, not only the fractional vortices are confined (logarithmically, with a prefactor of order U), but also the excitations that we argued are responsible for the microscopic dynamics, the open segments of closed two-color loops. The confinement of the two-color segments is proportional to the string length (linear) inside any ferromagnetically aligned domain, with a prefactor of order J. The example that we studied in this paper suggests an interesting scenario where defect confinement at the microscopic level is responsible for the slow dynamics and out-of-equilibrium behavior of a macroscopic system.

APPENDIX: MICROSCOPIC ORIGIN OF THE U AND J TERMS

In this appendix we estimate the relative values of U and J in terms of some microscopics for the tunneling through a Josephson barrier. Consider two neighboring triangles as in Fig. 3 sharing a common edge labeled by a. The microscopic tunneling Hamiltonian from a triangle labeled 1 to a neighboring triangle labeled 2 can be written as

$$H = -\sum_{\vec{k}, \vec{q}} t_{\vec{k}, \vec{q}} \, c_{\vec{k}}^{1\dagger} c_{\vec{q}}^2 + \text{H.c.} \tag{A1}$$

Using second-order perturbation theory, we can estimate from this expression the Josephson coupling between the two superconductors in a standard way. The result is

$$E_J \sim -\sum_{\vec{k},\vec{q}} \frac{|t_{\vec{k},\vec{q}}|^2}{E_\Delta} \langle c_{-\vec{k}}^{1\dagger} c_{\vec{k}}^{1\dagger}\rangle \langle c_{\vec{q}}^2 c_{-\vec{q}}^2\rangle, \qquad (A2)$$

where we used $t_{\vec{k},\vec{q}} = t_{-\vec{k},-\vec{q}}^*$ and E_Δ is the superconducting energy gap.

It is useful to define the angles $\phi_{\hat{k}}$ and $\phi_{\hat{q}}$ as those formed by the vectors $\vec{k}, \vec{q}$ and the reference unit vector $\hat{e}_{1,0}$. Notice that the ath unit vector $\hat{e}_{i,a}$ is normal to the side labeled by a (see Fig. 3 for the definition of these unit vectors).

The order parameters can be written as

$$\langle c_{-\vec{k}}^{1\dagger} c_{\vec{k}}^{1\dagger}\rangle = (\Delta_{\vec{k}}^1)^* = \Delta e^{-i(\theta_1 + \sigma_1 \phi_{\vec{k}})}, \qquad (A3)$$

$$\langle c_{\vec{q}}^2 c_{-\vec{q}}^2\rangle = \Delta_{\vec{q}}^2 = \Delta e^{i(\theta_2 + \sigma_2 \phi_{\vec{q}})}, \qquad (A4)$$

where Δ is the order parameter magnitude, $\theta_{1,2}$ are the overall phases of grains 1,2, and $\sigma_{1,2}$ are the chiralities of the $p \pm ip$ order parameter in each grain.

As we show below, the constants U and J strongly depend on the behavior of $t_{\vec{k},\vec{q}}$, which is in general very difficult to obtain from first principles. For a flat interface, the component of momentum parallel to the junction is conserved, i.e., $k_\parallel = q_\parallel$. If the momenta involved are close to the Fermi momentum (and assuming for simplicity a spherically symmetric Fermi surface), then one has (approximately) that $k_\parallel^2 + k_\perp^2 \approx k_F^2 \approx q_\parallel^2 + q_\perp^2$; hence, $k_\perp \approx q_\perp$ or $k_\perp \approx -q_\perp$, corresponding to forward and backward scattering in the normal direction to the barrier, respectively.

There should be a strong suppression of tunneling when the vectors $\vec{k}$, $\vec{q}$ are not normal to the interface. The reason is that the smaller the perpendicular component, the more exponentially suppressed is the tunneling amplitude (for example, consider a WKB approximation: the smaller $k_\perp$ and $q_\perp$, the lower the particle energy is with respect to the barrier). If $\delta\varphi$ is a small angle that measures deviations from normal incidence and $\phi_{\hat{e}_{1,a}} = (2\pi/3)a$, one can show that the main contribution to the Josephson tunneling Hamiltonian comes from choosing any of the following four combinations:

$$\phi_{\hat{k}} = \frac{2\pi}{3}a + \delta\varphi \quad \text{or} \quad \phi_{\hat{k}} = \frac{2\pi}{3}a + \delta\varphi + \pi \qquad (A5)$$

and

$$\phi_{\hat{q}} = \phi_{\hat{k}} \quad \text{or} \quad \phi_{\hat{q}} = \phi_{\hat{k}} + \pi - 2\delta\varphi, \qquad (A6)$$

where the last choice corresponds to forward or backward scattering, respectively.

The Josephson coupling can be written in terms of these choices as

$$E_J \sim -\frac{\Delta^2}{E_\Delta} \int d\delta\varphi [|t_F(\delta\varphi)|^2 \cos\{\theta_{1,a} - \theta_{2,a} + (\sigma_1 - \sigma_2)\delta\varphi\}$$

$$-|t_B(\delta\varphi)|^2 \cos\{\theta_{1,a} - \theta_{2,a} + (\sigma_1 + \sigma_2)\delta\varphi\}], \qquad (A7)$$

where $t_F(\delta\varphi)$ and $t_B(\delta\varphi)$ are forward and backward small-angle scattering amplitudes (also, recall the definition $\theta_{i,a} = \theta_i + (2\pi/3)a\,\sigma_i$ from Sec. II).

Expanding around small $\delta\varphi$ before carrying out the angular integral, one obtains

$$E_J \sim -[U + J\sigma_1\sigma_2] \cos(\theta_{1,a} - \theta_{2,a}), \qquad (A8)$$

where

$$U = \frac{\Delta^2}{E_\Delta} \int d\,\delta\varphi [|t_F(\delta\varphi)|^2 - |t_B(\delta\varphi)|^2](1 - \delta\varphi)^2 \qquad (A9)$$

and

$$J = \frac{\Delta^2}{E_\Delta} \int d\,\delta\varphi [|t_F(\delta\varphi)|^2 + |t_B(\delta\varphi)|^2]\delta\varphi^2. \qquad (A10)$$

As we discussed above, the barrier is more transparent for close to normal incidence, and can be engineered so that $\delta\varphi$ must remain small, and thus the ratio J/U as obtained above can be made controllably small. The precise condition for having $J \ll U$ depends on the details of $t_{F,B}(\delta\varphi)$. As a simple example, for tunneling through a square barrier in ordinary quantum mechanics, the ratio J/U will depend on the height of the barrier V and on $k_F a$, where a is the length of the barrier. The larger $k_F a$, the smaller J/U. This model may not capture in full detail the underlying physics of the Josephson coupling problem;[22] nevertheless, simple as it is, it shows how the structure of the barrier can be used to tune the ratio J/U.

If $J \ll U$, then in the temperature regime $J \ll T \ll U$ the system is effectively constrained to the three-color manifold of states: $\theta_{1,a} - \theta_{2,a} = 0 \pmod{2\pi}$. In this case, the effective Hamiltonian for the coupling between triangles 1 and 2 is simply

$$H_{1,2} = -J\sigma_1\sigma_2, \qquad (A11)$$

with $J > 0$ (ferromagnetic coupling).

[1] P.W. Kasteleyn, J. Math. Phys. **4**, 287 (1963).

[2] E.H. Lieb, Phys. Rev. Lett. **18**, 1046 (1967).

[3] R.J. Baxter, J. Math. Phys. **11**, 784 (1970).

[4] B. Chakraborty, D. Das, and J. Kondev, Eur. Phys. J. E **9**, 227 (2002).

[5] J. Kondev and C.L. Henley, Nucl. Phys. B **464**, 540 (1996); J. Kondev, J. de Gier, and B. Nienhuis, J. Phys. A **29**, 6489 (1996).

[6] V.G. Vaks, V.I. Zinenko, and V.E. Schneider, Usp. Fiz. Nauk **141**, 629 (1983) [Sov. Phys. Usp. **26**, 1059 (1983)]; V.G. Vaks and V.I. Zinenko, J. Phys. C **19**, 3083 (1986).

[7] A.P. Mackenzie and Y. Maeno, Rev. Mod. Phys. **75**, 657 (2003).

[8] There have been recent proposals of order parameters for Sr_2RuO_4 that have nodes along the c axis, but this possibility should not affect the results we discuss in this paper if the c axis is perpendicular to the triangles in the array. The only change is that the superconducting phases θ_i in each triangle will accommodate the sign changes of the order parameter (the phases will change by π) as a function of the vertical distance, along the

c-axis direction. For recent work on the *c*-axis nodes, see M.E. Zhitomirsky and T.M. Rice, Phys. Rev. Lett. **87**, 057001 (2001); H. Won and K. Maki, Europhys. Lett. **52**, 427 (2000); Hae-Young Lee, Yong Baek Kim, and K. Maki, cond-mat/0309156 (unpublished).

[9] J.E. Moore and D.-H. Lee, cond-mat/0309717 (unpublished).

[10] M.J. Higgins, Y. Xiao, S. Bhattacharya, P.M. Chaikin, S. Sethuraman, R. Bojko, and D. Spencer, Phys. Rev. B **61**, R894 (2000).

[11] Y. Xiao, D.A. Huse, P.M. Chaikin, M.J. Higgins, S. Bhattacharya, and D. Spencer, Phys. Rev. B **65**, 214503 (2002).

[12] K. Park and D.A. Huse, Phys. Rev. B **64**, 134522 (2001).

[13] P. Di Francesco and E. Guitter, Europhys. Lett. **26**, 455 (1994).

[14] D.A. Huse and A.D. Rutenberg, Phys. Rev. B **45**, 7536 (1992).

[15] Here by plaquette we mean any closed polygon of spins. The case of more complex spin plaquettes (e.g., with internal spins) requires some nontrivial adjustments in the CMFM.

[16] P. Di Francesco and E. Guitter, Phys. Rev. E **50**, 4418 (1994).

[17] H. Yin and B. Chakraborty, Phys. Rev. Lett. **86**, 2058 (2001); Phys. Rev. E **65**, 036119 (2002).

[18] J. Kondev and C.L. Henley, Phys. Rev. Lett. **74**, 4580 (1995).

[19] The more usual expression $E_{LQ} = c - a \tanh(b/T)$, used, for example, by Cavagna *et al.* (Ref. 20), provides a worse fit than Eq. (25) for our numerical data. Nevertheless, the difference in the transition temperatures derived with the two expressions is less than 0.5.

[20] A. Cavagna, I. Giardina, and T.S. Grigera, J. Chem. Phys. **118**, 6974 (2003).

[21] Z.W. Lai, G.F. Mazenko, and O.T. Valls, Phys. Rev. B **37**, 9481 (1988).

[22] See, for example, G.D. Mahan, *Many-Particle Physics*, 3rd ed. (Kluwer Academic, Dordrecht, 2000).